



UNIVERSITY OF CALIFORNIA, SAN DIEGO
DEPARTMENT OF APPLIED MECHANICS
AND ENGINEERING SCIENCES

SEISMIC STABILITY OF BLOCK STRUCTURES

by
Richard L. Furgerson

Report No. UCSD/AMES/TR-80/002

Prepared for the
National Science Foundation
Grant NSF PFR-78-16581

La Jolla, California

May, 1980

REPRODUCED BY
NATIONAL TECHNICAL
INFORMATION SERVICE
U.S. DEPARTMENT OF COMMERCE
SPRINGFIELD, VA 22161

EAS INFORMATION RESOURCES
NATIONAL SCIENCE FOUNDATION

UNIVERSITY OF CALIFORNIA, SAN DIEGO
Department of Applied Mechanics and Engineering Sciences
La Jolla, California 92093

SEISMIC STABILITY OF BLOCK STRUCTURES

by

Richard L. Furgerson

Any opinions, findings, conclusions
or recommendations expressed in this
publication are those of the author(s)
and do not necessarily reflect the views
of the National Science Foundation.

Report No. UCSD/AMES/TR-80-002

Prepared for the
National Science Foundation
Grant NSF PFR 78-16581

May 1980

TABLE OF CONTENTS

	Nomenclature	ii
	List of Figures	iv
	List of Tables	ix
	Abstract	x
I	Introduction	1
II	Observation of Structural Subassembly Dislocation and Collapse Due to Kinetic Instability	3
III	Friction Law	8
	Derivation of the Friction Law	10
	Features of the Friction Law	14
IV	Prototype One-Degree-Of-Freedom Structure	16
	Description of the Prototype One-Degree- Of-Freedom Model	16
	Mathematical Model and Numerical Solution Technique	16
	Acceleration Function	19
	Results and Discussion	21
V	Practical Application of Results From One-Degree- Of-Freedom Model	23
VI	Two-Degree-Of-Freedom Model Allowing Planar Motion of Floor Slab	30
	References	35
	Appendix	76

NOMENCLATURE

$a(\tau)$	prescribed nondimensional acceleration, $a = \frac{d^2}{d\tau^2} y(\tau)$
a_{\max}	$\max_{\tau>0} a(\tau) $
$a_v(\tau)$	prescribed dimensionless acceleration of the assemblage in the up direction
$a_x(\tau)$	prescribed dimensionless horizontal acceleration of the base perpendicular to the plane of the walls
$a_y(\tau)$	prescribed dimensionless horizontal acceleration of the base parallel to the plane of the walls
d	width of the wall (feet)
f	frequency of base oscillation (Hz.)
f_x	$\omega_x/2 t^*$
f_y	$\omega_y/2 t^*$
g	acceleration of gravity (32.2 ft/sec ²)
t	time (seconds)
t^*	a characteristic time defined by $(d/(2g))^{1/2}$
$u(\tau)$	relative horizontal displacement between the wall and the floor slab
$x_b(\tau)$	dimensionless horizontal displacement of the base perpendicular to the plane of the walls from its $\tau = 0$ location
$x_s(\tau)$	dimensionless horizontal displacement of the slab perpendicular to the plane of the walls from its $\tau = 0$ location
$y(\tau)$	prescribed nondimensional displacement of base
$y_b(\tau)$	dimensionless horizontal displacement of the base parallel to the plane of the walls from its $\tau = 0$ location
y_{\max}	$\max_{\tau>0} y(\tau) $
$y_s(\tau)$	dimensionless horizontal displacement of the slab parallel to the plane of the walls from its $\tau = 0$ location

A	the maximum amplitude of the prescribed horizontal acceleration (g's)
α, β	parameters controlling the shape of the acceleration envelope
$\delta(\tau)$	nondimensional relative displacement, $u/(d/2)$ nondimensional frequency, $2\pi ft^*$
ω_x	dimensionless frequency of the prescribed acceleration function in the direction of $a_x(\tau)$
ω_y	dimensionless frequency of the prescribed acceleration function in the direction of $a_y(\tau)$
γ_c	collapse factor proportional to $(\tau_c)^{-1}$
τ	nondimensional time, t/t^*
τ_c	value of τ at collapse
τ_{dur}	value of τ at which the prescribed displacement envelope decreases to half maximum amplitude
τ_{max}	value of τ at maximum of the acceleration envelope
τ_{rise}	value of τ at which the prescribed acceleration envelope first attains half maximum value
μ	friction ratio: frictional force/normal force

LIST OF FIGURES

Figure		Page
1	A monument, rotated on its base, after the Managua, Nicaragua earthquake, December 23, 1972. ⁵	37
2	A toppled monument after the Managua, Nicaragua earthquake, December 23, 1972. ⁵	37
3	The boiler room of the Olive View Hospital after the San Fernando earthquake of February 9, 1971. The angle of the plumbing attached to the boiler, vertical before the earthquake, gives an indication of the sliding that took place. ⁶	38
4	Skid marks showed that this heavy lathe slid 9 feet across the machine shop floor during the San Fernando earthquake, February 9, 1971. ⁶	38
5	The first floor of the Psychiatric Day Care Center collapsed, the second floor is shown intact. Olive View Hospital after the San Fernando earthquake, February 9, 1971. ⁷	39
6	A shear wall in a multi-story building shows displacements at construction joints after the San Fernando earthquake, February 9, 1971. ⁷	39
7	An intact stairwell has toppled at the Olive View Hospital after the San Fernando earthquake, February 9, 1971. ⁷	40
8	The penthouse of this hotel rotated during the Managua, Nicaragua earthquake, December 23, 1972. ⁷ ..	40
9	The same penthouse as in Figure 8 viewed from a different angle. ⁵	41
10	The roof channels of the homes in this tract slipped off their supporting walls in similar ways during the Managua, Nicaragua earthquake, December 23, 1972. ⁵	41

11	The roof channel of this home slipped some inches to the left during the Managua, Nicaragua earthquake, December 23, 1972. The dark area on the underside of the roof channel formerly bore on the supporting wall, the light area is the ceiling paint of the room through the door to the right. ⁵	42
12	Orientation of the block hollows for the bed joint and the head joint.	43
13	Concrete masonry half-block triplet in static shear test after joint fracture. (Bed joint illustrated, displacement exaggerated).	44
14	Concrete masonry half-block (7 5/8" x 7 5/8" x 7 5/8") triplet in static shear test. A perspective of the undeformed specimen in fixture.	45
15	Typical experimental curves of total shear load V vs. deflection δ ; δ is measured from unloaded state. (Data points are sample mean values of V at each δ ; the half-height of the vertical bar equals the unbiased estimate of the standard deviation for the sample. In each case, sample size was 3 runs.)	46
16	Variation of standard deviation vs. sample mean for several different tests.	47
17	Minimization of f_m as function of V_∞ in a typical case (BJ-F-G-400) with $\alpha = 2$, and two values of β	48
18	Comparison of model with experiment for the fully-grouted bed joints.	49
19	Comparison of model with experiment for the ungrouted bed joint (mortar only).	50
20	Comparison of model with experiment for the fully-mortared head joint.	50

21	Predicted linear relation between frictional stress $\tau_{\infty} \equiv V_{\infty}/A$ vs. confining pressure CP for three cases of masonry joints.	51
22	Bidirectional shearing force versus center block displacement for 3 cycling rates where the maximum center block velocities vary over a 40 to 1 range.	52
23	Configuration of the idealized wall-floor slab assemblage.	53
24	Comparison of the accelerograms recorded on the ground floor and on the 10th floor of 6200 Wilshire Blvd. February 9, 1971.	53
25	The spectral decomposition of the Pacoima Dam, February 9, 1971, S14W component of acceleration. The modulus of the Fourier coefficients normalized so that the largest component is 1 vs. frequency.	54
26	The spectral decomposition of the absolute acceleration of a linear oscillator, damping = 2% critical, undamped natural frequency = 1 Hz., excited by the Pacoima Dam, February 9, 1971, S14W acceleration component input. The modulus of the Fourier coefficients normalized so that the largest component is 1 vs. frequency.	54
27	The absolute value of absolute acceleration of a linear oscillator, damping = 2% critical, undamped natural frequency = 1 Hz. due to the Pacoima Dam February 9, 1971 S14W component of acceleration with the moderately rising envelope superimposed vs. time.	55
28	Surface $\gamma_c(A,f)$ for the scaling parameter τ_{max} , $\gamma_c \equiv \tau_{max}/\tau_c$, computed with the base acceleration contained in a fast rising envelope.	56

29	Surface $\gamma_c(A, f)$ for the scaling parameter τ_{\max} , $\gamma_c \equiv \tau_{\max} / \tau_c$, computed with the base acceleration contained in a moderately rising envelope.	56
30	Surface $\gamma_c(A, f)$ for the scaling parameter τ_{\max} , $\gamma_c \equiv \tau_{\max} / \tau_c$, computed with the base acceleration contained in a slowly rising envelope.	57
31	Surface $\gamma_c(A, f)$ for the scaling parameter τ_{rise} , $\gamma_c \equiv \tau_{\text{rise}} / \tau_c$, computed with the base acceleration contained in a fast rising envelope.	57
32	Surface $\gamma_c(A, f)$ for the scaling parameter τ_{rise} , $\gamma_c \equiv \tau_{\text{rise}} / \tau_c$, computed with the base acceleration contained in a moderately rising envelope.	58
33	Surface $\gamma_c(A, f)$ for the scaling parameter τ_{rise} , $\gamma_c \equiv \tau_{\text{rise}} / \tau_c$, computed with the base acceleration contained in a slowly rising envelope.	58
34	Nondimensional collapse time τ vs. amplitude A given fixed frequency $f = 0.75$ Hz. and moderately rising acceleration envelope.	59
35	Nondimensional relative displacement $\delta(\tau)$ vs. nondimensional time τ with acceleration envelope vs. nondimensional time τ for $A = 1.0$, $f = 1.125$ Hz. and moderately rising acceleration envelope.	59
36a	Floor slab-shear wall configuration for the planar motion model.	60
36b	Top views of floor slab-shear wall configuration for the two-degree-of-freedom model at $\tau = 0$ (dotted lines) and at some later time τ_1 , $\tau_1 > 0$ (solid lines). ..	61
37	Surface $\gamma_c(A_x, f_x)$, $\gamma_c \equiv \tau_{\max} / \tau_c$. The result from the planar motion model with the moderately rising acceleration envelope, $A_y := 0.9 A_x$ and $f_y := 0.2$ Hz.	62

38	Surface $\gamma_{c_x}(A_x, f_x)$, $\gamma_c \equiv \tau_{\max} / \tau_c$. The result from the planar motion model with the moderately rising acceleration envelope, $A_y := 0.9 A_x$ and $f_y := 0.5$ Hz.	63
39	Surface $\gamma_{c_x}(A_x, f_x)$, $\gamma_c \equiv \tau_{\max} / \tau_c$. The result from the planar motion model with the moderately rising acceleration envelope, $A_y := 0.9 A_x$ and $f_y := 1.0$ Hz.	64
40	Surface $\gamma_{c_x}(A_x, f_x)$, $\gamma_c \equiv \tau_{\max} / \tau_c$. The result from the planar motion model with the moderately rising acceleration envelope, $A_y := 0.9 A_x$ and $f_y := 2.0$ Hz.	65
41	Surface $\gamma_{c_x}(A_x, f_x)$, $\gamma_c \equiv \tau_{\max} / \tau_c$. The result from the planar motion model with the moderately rising acceleration envelope, $A_y := 0.9 A_x$ and $f_y := 5.0$ Hz.	66
42	Surface $\gamma_{c_x}(A_x, f_x)$, $\gamma_c \equiv \tau_{\max} / \tau_c$. The result from the planar motion model with the moderately rising acceleration envelope, $A_y := 0.9 A_x$ and $f_y := 10.0$ Hz.	67

LIST OF TABLES

Table		Page
1	Raw test data used for correlation: total shear force V_i (kips) vs. ram displacement δ_i (inches) (measured from ram displacement at peak load) test runs in three cases, BJ-F-G, BJ-F-NG, and HJ-F-NG, and for confining pressure CP = 100, 200, 300, 400, 500 (psia) in each case.	68
2	Summary of best-fit values for regression parameters V_∞ , c, and b, fitted to the sample mean values of V_i for each test, for three cases and five confining pressures.	71
3	Statistical analysis of 7 runs of test BJ-F-NG-200. ...	72
3a	Calculation of regression parameters V_∞ , c, and b for each run, and comparison of the figures of merit f_m for $\alpha = 2$, $\beta = 0$, and for $\alpha = 2$, $\beta = 1/3$	72
3b	Comparison of values obtained for regression parameters V_∞ , c, and b as determined by: i) means of values as calculated from each of 7 runs in Table 3a ii) means of values as calculated from each of 6 runs (omitting run #7) in Table 3a iii) sample mean values for 7 runs: see below iv) sample mean values for 6 runs (omitting run #7--same values as in Table #2): see below	73
3c	Confidence intervals for mean \bar{V}_∞ , variance $\hat{\sigma}^2$, and standard deviation $\hat{\sigma}$ for V_∞ as calculated for each run in a sample size of 6 runs (omitting run #7). ...	74
4	The correspondence between the chosen nondimensional characteristic times and real time for an "8 inch" wall, $t^* = 0.099$	75

SEISMIC STABILITY OF BLOCK STRUCTURES

by

Richard L. Furgerson

Abstract

When studying earthquake damaged reinforced concrete or concrete masonry structures, it has been observed that the mechanisms of failure are often simple ones; the vulnerable connections between structural components degrade under stress allowing the major substructures to separate, lose support and topple. This type of failure is said to result from kinetic instability. For the purpose of analysis, structures with degraded connections are modeled as assemblages of rigid substructures with only friction acting between them. A statistical analysis of data from experiments on concrete masonry members gives an asymptotic Coulomb law describing this friction which is included in the model equations of motion. The equations of motion for a simple shear-wall-floor slab assemblage subjected to simulated earthquake loading are solved numerically. The result shows a surprisingly well-defined relation between the maximum amplitude of excitation, the natural frequency of the structure, and a numerically-valued hazard from kinetic instability. When presented graphically, the result allows a designer to assess hazard from kinetic structural instability by inspection.

I INTRODUCTION

Beginning in the era of Newton and the Bernoullis, some of the most elegant treatments in classical mechanics and applied mathematics have resulted from efforts to describe the motion of rigid bodies under force. This has lead to a mature theory with widespread application. One of these is the description of the motion of structures subject to very high loading, such as intense seismic loading.

The devastation caused by a severe earthquake near a populated area shows all too clearly that the component parts of structures undergo gross deformations very large compared to any deformation in the elastic range of the material. While it is now possible with the use of large computers to analyse the detailed anelastic response including cracking of structures which would lead to structural collapse, these methods are very complex. Instead, a simpler model is proposed and demonstrated in the present work: ignore elastic deformation and model the structure as an assemblage of rigid elements which have friction acting between them. Given a realistic friction law, the equations of motion for the assemblage of rigid elements subjected to earthquake loading can be solved. This model is regarded as the result of prior degradation of the actual structure. Although severe damage has occurred, the degraded structure is initially able to carry its primary loads.

An analysis of experimental data shows that a Coulomb type friction is a satisfactorily accurate model of the inter-element friction for structures made from concrete masonry. Coulomb friction, also called solid friction, models the frictional force between bodies moving relative to each other as being the product of a constant friction coefficient and the normal force across the sliding joint. When the forces acting in a direction so as to cause relative motion between two bodies do not exceed

the product of the friction coefficient and the normal force, the frictional reaction balances any forces that would tend to cause relative motion so that there is no sliding. The simplified friction model used here does not distinguish between static and dynamic friction.

Analytical treatment of dynamical problems involving Coulomb friction have been briefly considered by a few authors: Den Hartog¹ discusses replacing the Coulomb friction with an energy equivalent viscous friction, sidestepping the stick-slip nature of the problem; Ziegler² points out some of the non-intuitive types of behavior that Coulomb-damped oscillators may demonstrate such as the fact that a Coulomb damped oscillators may still undergo an unbounded response; Frazer, Duncan and Collar³ discuss the implication of the presence of stick-slip or ankylotic motion of control surfaces to the stability of aircraft. None of these authors treat the problem of kinetic structural stability.

The mechanical nature of the solution of problems involving Coulomb friction makes them more suitable for automatic computation than for analytical examination. Numerical techniques are used in the present work to solve a simple prototype structural stability problem involving a rigid body shear-wall floor slab configuration with Coulomb friction acting between the vertical and horizontal elements (see Fig. 36). Motion of the base is excited by a simulated seismic loading. This assemblage is said to be kinetically stable if the floor slab in responding to the excitation does not fall off its supporting shear-walls which would define collapse. Hazard from collapse due to kinetic instability is taken as being inversely proportional to the time the assemblage can withstand the excitation before collapsing. The results present the computed hazard of collapse as a function of maximum amplitude and frequency of excitation in graphical form, allowing assessment by inspection of hazard due to collapse.

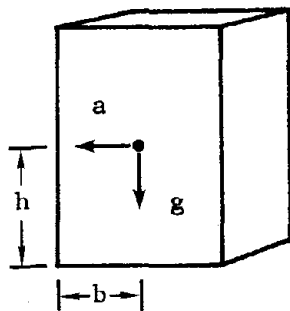
II OBSERVATION OF STRUCTURAL SUBASSEMBLY DISLOCATION AND COLLAPSE DUE TO KINETIC INSTABILITY

Following definitions given in Chapter I, a kinetically stable structural system of rigid elements can be thought of as an assemblage of elements none of which will collapse or overturn due to specified forces acting on the assemblage, although the elements may undergo substantial relative motions. For the purposes of this paper, concrete or masonry building structures are the assemblages of elements considered. Whether or not an assemblage is kinetically stable can be determined by considering the relative displacements, velocities, and the inertial properties of its substructures and the the forces applied to them.

Reinforced concrete or masonry structures are built up of subassembly elements. Often this is purposeful as in prefabricated, prestressed modules which can be used to advantage where a standard-shaped section is required. Indeed, even structures monolithic in appearance have in them inadvertant construction joints because building construction does not progress continuously. See discussion of Fig. 6 below. As far as seismic analysis is concerned, the idea that buildings are assemblages of substructures is important because experience with structures subject to earthquake ground motion has shown engineers that the connections between substructures are particularly vulnerable to seismic degradation. It is seen that once these bonds are broken, the substructures are free to move independently, and the building can be considered an assemblage of rigid elements. Often these elements have simple geometries.

In fact, the idea of kinetic stability served as the basis for one of the first methods used to quantify the strength of earthquake acceleration. According to Kirkpatrick⁴, Mallet was perhaps the first to suggest that the stability of common objects might serve as an empirical scale by which investigators might rank earthquake strength after surveying the damage. When reading the old accounts, one finds strengths compared relatively

as certain percentage of chimneys fallen within a given area or by percentage of gravestones overturned. Because such methods removed the seismologists' dependence on the subjective judgement of untrained witnesses for a strength estimate, an amount of attention was given to the problem of the overturning of blocks by horizontal accelerations in the literature. Again, Kirkpatrick⁴ states that Milne and Omori in 1885 reported experiments suggesting an empirical multiplicative factor to correct the West formula, $a=(b/h)g$, for overturning of blocks by horizontal acceleration.



a = minimum overturning horizontal acceleration

g = acceleration of gravity

h = block half-height

b = block half-width

They actually used this method to investigate earthquakes in Japan, where lanterns and monuments are generously distributed. It was realized that static considerations alone were not sufficient to establish kinetic stability, but this procedure was carried on with some refinement for years (Kirkpatrick⁴). Of course, overturning of monuments is still seen. Figs. 1 and 2 show monument stones overturned or displaced after the Managua earthquake. The overturning of blocks is a type of rigid body or kinetic instability.

A number of descriptions of earthquake induced rigid body motions and structural failures follow, illustrating the variety of forms kinetic instability through rigid body motion may take. Reference 6 contains many excellent photographs of additional examples such as Figs. 3.10-3.13.

Machines such as those providing heating and air conditioning to buildings frequently translate as rigid bodies substantial

distances during earthquakes if not securely anchored to the floor. Fig. 3 shows a massive boiler at the Olive View Hospital coming to rest 4 feet from its original position after the San Fernando earthquake. Similarly, a heavy lathe in a machine shop is found to have have translated 9 feet from its original location. Fig. 4.

An example of stability of rigid subassemblies is seen in Fig. 5. During the San Fernando event, high loads degraded the moment resisting capacity of the columns supporting the second story of the Psychiatric Day Care Center of the Olive View Hospital until the structure was reduced to a mechanism. The second floor collapsed as a rigid substructure onto the first. The photograph shows the second floor fairly intact. Much of the glasswork in the second floor is unbroken. As mentioned above, seemingly monolithic structural elements contain internal joints between material placed on different days during construction. Restraints on the size and strength of concrete forms due to handling and economic considerations usually limit the depth concrete may be poured to less than 10 feet; a tall shear wall may have many such construction joints. Fig. 6 is a photograph of a tall shear wall in a multi-story building after the San Fernando earthquake. The horizontal cracks at the construction joints are clearly visible. Permanent horizontal displacements in excess of 1/4 inch were observed.

The simple modular geometry of stairwells and elevator shafts very much resemble the blocks for which Professor West developed his overturning formula. Often these subassemblies are constructed with only light connection to the parent structure. Under earthquake excitation of the structure, the connections fail allowing the stairwell to move as an independent rigid body. Being a tall, slender substructure, the stairwell may overturn. Fig. 7 shows a quite intact stairwell after being overturned during the San Fernando earthquake. The stability of stairwells is not just a problem confined to the Southern California locale, similar stairwell failures occurred during the Managua and Anchorage

earthquakes.

When subjected to earthquake ground motion, reinforced concrete roadway bridges can exhibit one of the simplest rigid body instabilities. The span simply slips off its supporting abutments. The span is necessarily not connected to its abutments to accommodate expansion and contraction due to temperature changes.

Structural separation into rigid, independent subassemblies sometimes divides the structure into a few, quite simple, rigid substructures. A case in point is seen in Fig. 8 and 9. After the Managua earthquake, the penthouse on top of the pictured luxury hotel is seen to have undergone a permanent rotation and translation. Had the rotations and displacements been larger, the penthouse could have slipped off the top floor and fallen; its kinetic stability could be in question.

In a residential section of Managua, a tract of nearly identical homes was built. The walls were reinforced concrete, the roofs were made of a number of prefabricated concrete channel sections. Apparently, these channel sections were not secured to the walls. During the earthquake, many of the channels slid off their supporting walls in precisely the same way, Fig. 10. This photograph shows the similarity of failure. Fig. 11 shows a roof section, while not failing, displaced some inches from its original position. The darker unpainted portion of the bottom of the channel originally bore on the supporting walls; the lighter portion is the ceiling paint of the room on the other side of the wall. While in a majority of instances, the walls and the roof sections remained individually intact as substructures, these subassemblies making up the homes moved relative to one another to the extent as to become kinetically unstable.

Since the walls and roof sections can be modeled simply and realistically, the geometry of Fig. 11 is the basis for the prototype two-body problem: Describe the motion of a slab of

reinforced concrete material supported on rigid walls of concrete masonry, where the walls are built into a base which undergoes a prescribed vertical and horizontal acceleration. The prototype problem is analysed in later chapters.

Before solving the equations of motion of the prototype assemblage, it is necessary to prescribe the tractions on the interfaces between these rigid bodies. Particularly significant is the interface friction between the elements sliding against one another. If realistically modeled, the character of the chosen friction law can contribute substantial complexity to the equations of motion.

III FRICTION LAW

In order to pose the equations of motion for the prototype assemblage, the frictional behavior of abrading cementous interfaces must be described. In connection with the UCSD Masonry program (Reference 9 contains contributions by UCSD Masonry program investigators which may serve as a project overview), frictional behavior as well as material strengths of masonry were studied. Data from the program's experiments produced a simple, realistic friction law with the following properties:

- (1) The frictional stress along the interface and the normal stress on the interface have an asymptotic Coulomb relationship for large total displacements.
- (2) The law is bidirectional.
- (3) The law is sliding rate independent.

Property (1) is demonstrated by the result of a statistical analysis of data taken during a number of experiments. Properties (2) and (3) were observed empirically from data taken during a number of experiments. A description of the experiments investigating the elastic, fracture, and post-fracture response of masonry assemblages, and the analysis of the resulting data leading to the friction law, follows.

The specimens tested were assemblages of 3 half-blocks, triplets, constructed by professional masons working under field conditions using typical materials, materials meeting relevant standards for quality and strength. The diagram in Fig. 12 shows a triplet that blocks are joined with one of the two basic mortar joints: The bed joint or the head joint. These are the first 2 specimen configurations tested. Filling the hollow in the bed joint triplet with a fluid concrete, called grout, results in the third configuration subjected to test in this phase of the program.

The 3 half-block assemblage was chosen since it is a manageable size and does not require a machine of extraordinary capacity to apply failure loads. The configuration is also used by contractors in the field to prove that required strength of the masonry has been attained, satisfying building code regulations. Reference contains a complete description of the manufacture of the specimens including relevant ASTM standards for the materials and information about the curing procedure.

Two loads are applied to the triplet. A load acting perpendicular to the long dimension, the vertical load, displaces the center block while a constant load, acting in the ends forcing the blocks together, is maintained by additional hydraulic equipment, Figs. 13 and 14. Considerable attention is paid to distributing the loads uniformly over their active surfaces, Figs. 13 and 14. The triplet is bedded with a thin layer of Hydrocal plaster to a substantial aluminum base plate. A steel bearing plate is similarly bedded to the top of the center block. The confining load, load applied to the ends, is distributed via a stiff steel plate and neoprene pad to insure uniformity. The reader is directed to Ref. 9 for a detailed discussion of the mounting and loading procedure including photographs of the test setup.

As the displacement of the center block, δ , increases, shear failure occurs along the mortar joints for confining loads below a critical value. Since the vertical load is resisted by a shearing action across the mortar joints of the triplet, the vertical load will be called the shearing force, V . Shearing force vs. vertical displacement of the center block data were taken for a number of tests at each of five confining loads and each of the 3 configurations. For two different confining loads, Fig. 15 illustrates the curve obtained by averaging all the data taken from specimens of one configuration tested at one confining load. The load versus displacement data for any one

test can be divided into three regions: (i) a linear elastic region, (ii) a non-linear region, and (iii) a post-fracture, sliding region. The subsequent investigation confines itself to the post-fracture, sliding region.

DERIVATION OF THE FRICTION LAW

The decaying behavior of the shear force versus displacement data in the post-fracture region suggests that the shearing force may be modeled there by solutions, $V(\delta)$, of this differential equation:

$$(1) \quad \frac{dV(\delta)}{d\delta} = -\bar{c} (V(\delta) - V_{\infty})$$

V_{∞} is the value to which $V(\delta)$ decays after sliding over a large displacement. Since the energy of the shearing force acting through the displacement, δ , is dissipated by grinding and smoothing of the blocks at the fracture interface, the parameter \bar{c} in Equation (1) could depend on the work $W(\delta)$ done by interface friction acting through a displacement, δ .

$$W(\delta) = \int_{\delta_1}^{\delta} V(\delta') d\delta'$$

For each configuration and confining load, the data were averaged to produce a mean curve as in Fig.15. For the purpose of fitting the data to the following general solution to Equation (1),

$$(2) \quad \frac{V(\delta) - V_{\infty}}{V_1 - V_{\infty}} = \exp \left[- \left(c \int_0^{\delta} (W(\delta'))^{\beta} d\delta' + b \right) \right]$$

samples, V_i , from the averaged data curves were taken at $i = 1, \dots, 9$ evenly spaced displacements, δ_i , measured beginning from the center block displacement corresponding to the maximum shear force.

$$\delta_1 \equiv 0$$

$$\delta_9 = 0.4 \text{ inches}$$

The constants c , b , and V_∞ are regression parameter determined by an extremum procedure. The constant, β , is chosen equal to 0 or 1/3 whichever gives the best result. The case of $\beta = 1/3$ is included to accommodate a possible volumetric effect. The regression parameters c and b are determined from the data by minimizing a quadratic form, $M(c,b,V_\infty)$, defined by the following set of equations for $i = 1, \dots, 9$:

$$\xi_i \equiv \int_0^{\delta_i} (W(\delta'))^\beta d\delta'$$

$$\eta_i \equiv \log \left[\frac{V_1 - V_\infty}{V_i - V_\infty} \right]$$

$$\bar{\eta}_i \equiv c\xi_i + b$$

$$M(c,b,V_\infty) \equiv \sum_{i=1}^9 (V_i - V_\infty)^\alpha (\eta_i - \bar{\eta}_i)^2$$

The value of α is chosen to be 0 or 2. A result from the statistical theory of linear regression suggests that $\alpha = 2$ is appropriate if the standard deviation of the samples of the individual data at a given δ_i used to generate the mean curve varies with the sample mean and that $\alpha = 0$ is appropriate if the standard deviation is constant, Ref. 10. Fig. 16 shows how the standard deviation varies with sample mean for one of the triplet configurations. The standard methods of the linear regression of η and ξ enable c and b to be determined explicitly as functions of V_∞ through solution of the pair of equations (3,4).

$$(3,4) \quad \frac{\partial M}{\partial c} = 0 \quad \frac{\partial M}{\partial b} = 0$$

These expressions for c and b in terms of V_∞ permit the residual

sum of squares divided by n , a quantity called f_m ,

$$(5) \quad f_m \equiv \frac{1}{n} \sum_{i=1}^n (V_i - V(\delta_i))^2$$

to be expressed as a function of V_∞ only. $V(\delta)$ is given by Equation (5) in which the only remaining unknown is the regression parameter V_∞ . A computation determines the V_∞ which minimizes f_m . Fig. 17 shows an example of V_∞ versus f_m .

For each prescribed triplet configuration and confining load condition, a number of specimens were tested and their data averaged. The model fitting procedure was applied to samples from the averaged data. The results of the fitted $V(\delta)$ vs. δ for various confining pressures (CP) are shown in the following figures:

Fig. 18 Bed joint grouted CP = 100, ..., 500 psi

Fig. 19 Bed joint ungrouted CP = 100, ..., 500 psi

Fig. 20 Head joint CP = 100, ..., 400 psi

CP equals the confining load divided by the appropriate bearing area, A_b . In these figures, the full lines indicate values of $V(\delta)$ in the post-fracture, sliding region, the applicable region for the model. The dotted lines indicate the trend of the experimental data prior to bond fracture. The fit is seen to be quite good.

The essential feature of this model is the form of the behavior of V_∞ vs. confining pressure. This behavior is shown for all three configurations in Fig. 21. In order to use the test data as a point relation between surface shearing stress and lateral pressure, V_∞ is divided in each instance by the appropriate bearing area, A_b , to show τ_∞ on the ordinate of Fig. 21. For $CP \leq 400$ psi, the data is in very good agreement with the form of the Coulomb or or the Amonton Law for sliding friction,

$$\tau_\infty = \mu_\infty CP$$

for constant coefficient of friction, μ_∞ . The values of τ_∞ for

$CP = 500$ are seen to correspond poorly. However, it was observed that

the tests for this high confining pressure resulted in block spalling and severe block cracking. This failure mode was unlike the clean bond fracture and sliding failure seen in the lower confining pressure experiments. Thus, the model, Equation (1), which relies on the plane interface sliding assumption is inappropriate for describing the results for the CP = 500 psi tests, and the CP = 500 psi result is omitted from the calculation of μ_{∞} .

The results for the two types of joints having mortar only are quite close, Fig. 21, while the value of μ_{∞} for the grouted joint is somewhat larger. The least-squares slopes, μ_{∞} , for the τ_{∞} vs. CP data were calculated.

$$\mu_{\infty} = 0.55 \text{ for BJ-F-NG}$$

$$\mu_{\infty} = 0.60 \text{ for HJ-F-NG}$$

$$\mu_{\infty} = 0.66 \text{ for BJ-F-G}$$

There were usually 3 specimens tested for each confining pressure and triplet configuration. The data curves for each confining pressure and triplet configuration are then averaged to form a composite curve which is then fitted to the sliding friction model. To establish the validity of the use of the composite curve to generate the asymptotic friction law for the interface, i.e. Coulomb friction, the case of BJ-F-NG with CP = 200 psi was subjected to a statistical analysis. For this particular case, 7 specimens were tested. The value of V_{∞} was calculated for each of the individual data curves. The result of that calculation appears in Table 3. It can be seen that the value of V_{∞} calculated from test #7 is conspicuously greater than the other values. If some sort of testing error or operator mistake were responsible for this irregularity, this point could be omitted from further analysis. Nevertheless, in this instance, the discrepancy cannot be attributed to obvious experimental mistakes. However, statistical tests have been devised to indicate the likelihood that an "outlier", an experimental value distant from other supposed similar data, is not drawn from the same population as the other data.

Appendix 2 describes the procedure for challenging an "outlier" on statistical grounds.

The results of this procedure show that within 95% confidence the value of V_{∞} given in test #7 does not belong to the same population as the other values. The "outlier" is then excluded from the final analysis. Table 4 shows the result of fitting the BJ-F-NG CP = 200 psi composite curve with and without including Test #7. Note that the value of V_{∞} (Table 4) from fitting the composite curve (excluding Test #7) is in very good agreement with the average of the V_{∞} values resulting from the fitting of the individual data justifying the use of the composite curves only for the computation of V_{∞} for the other cases of confining pressure and triplet configuration.

Another series of experiments on triplets was performed using more sophisticated test equipment, Ref. 8, which was capable of forcing bidirectional displacements of the center block. The displacement of the center lock could be a prescribed function of time. Shearing force vs. center block displacement data were taken where the displacement was prescribed to be a sinusoid, the frequency of which was varied resulting in the maximum velocity of the center block varying over a 40 to 1 range. Figure 22 shows the resulting shearing force vs. center block displacement data. The magnitude of the shearing force is seen to be constant--independent of direction of motion or sliding velocity. Further unidirectional tests having center block velocities varying over a 10 to 1 range corroborate the sliding velocity independence of the shearing force.

FEATURES OF THE FRICTION MODEL

In summary, model fitting the experimental results produces an interface sliding friction relationship for normal pressures of less than 400 psi. The description asymptotic

Coulomb is used to be suggestive of the fact that the interface sliding friction law approaches a Coulomb law as the sliding distance increases. In practice, it is seen that after relative interface sliding a total distance of only about 0.4 inches, the sliding friction relationship is closely approximated by a Coulomb friction law with constant coefficient. The friction coefficient is not dependent on the rate or direction of sliding.

IV PROTOTYPE ONE-DEGREE-OF-FREEDOM STRUCTURE

Although from a very simple model structure, the result of the following analysis will be shown to indicate the major features and trends of a class of hazard prediction problems.

DESCRIPTION OF THE PROTOTYPE ONE-DEGREE-OF-FREEDOM MODEL

Consider a structure similar to that pictured in Fig. 11 modeled as a rigid floor slab supported by two rigid, parallel shear walls built into a rigid base, Fig. 1. The floor slab has no connection to the shear walls, and interface friction alone causes the floor slab to move with the walls. The previous analysis of sliding concrete block experiments shows that Coulomb friction with a constant coefficient, $\mu = 0.6$, is an appropriate friction condition to prescribe¹¹. One degree-of-freedom is permitted, translation of the floor slab in a direction out of the plane of the walls. A prescribed horizontal acceleration, $a(\tau)$, simulating seismic loading acts on the walls and base.

MATHEMATICAL MODEL AND NUMERICAL SOLUTION TECHNIQUE

Including Coulomb friction with its stick-slip character introduces significant complications in the integration of the equations of motion. Heretofore, the substitution of an "equivalent" viscous or velocity dependent friction law to render the equations of motion more tractable analytically has been made. By contrast, this work relies wholly on numerical methods to track the stick-slip status of the assemblage and to integrate the unsimplified equations of motion.

The floor slab begins slipping on the walls when the magnitude of the base acceleration in g's exceeds the friction coefficient, if the slab is sliding over the walls, it will stop sliding if the magnitude of the base acceleration in g's is less than the friction coefficient and the velocities of the slab and walls are equal. The describing equations expressed in nondimensional quantities follow:

Let

$y_s(\tau)$ = nondimensional displacement of the floor slab
from its $\tau = 0$ location

$y_b(\tau)$ = nondimensional displacement of wall from its
 $\tau = 0$ location

$y_s(\tau) = \dot{y}_s(\tau) = y_b(\tau) = \dot{y}_b(\tau) = 0$ at $\tau = 0$

Equations for sticking are:

$$\left. \begin{array}{l} \ddot{y}_b(\tau) = a(\tau) \\ \ddot{y}_s(\tau) = a(\tau) \end{array} \right\} \text{ if floor slab is not sliding on the walls.}$$

The floor slab will be sliding at $\tau = \tau_1$, say, if and only if
 $|a(\tau_1)| > \mu$. During sliding, the governing equations are

$$\left. \begin{array}{l} \ddot{y}_b(\tau) = a(\tau) \\ \ddot{y}_s(\tau) = -\mu \operatorname{sgn}(\dot{y}_s - \dot{y}_b) \end{array} \right\} \text{ if floor slab is sliding on the walls for } \tau_1 \leq \tau < \tau_2.$$

Once sliding, floor slab will have stopped sliding at $\tau = \tau_n$,
 $\tau_n > \tau_1$ if and only if the following two conditions are met:

$$|a(\tau_n)| < \mu \quad \text{and} \quad \dot{y}_b(\tau_n) = \dot{y}_s(\tau_n)$$

A brief description of the solution technique follows;
Appendix I contains complete details of the code.

The integration of the initial value problem proceeds by marching, with a polynomial approximation of the slab and wall velocities updated at each time step. Tests for changes in motion regime, slipping or sticking, are then performed on the solution.

If the slab and walls were sticking at the previous time step, the magnitude of the acceleration is computed. If the magnitude of the acceleration is less than μ , the motion regime is unchanged, still sticking, and the solution is again advanced a time step. If the magnitude of acceleration is larger than μ , then slipping begins at some time between the current solution time and the last solution time. A Newton iteration calculates the time at which slipping begins, such a time τ being characterized by:

previous time $< \tau <$ present time such that $|a(\tau)| = \mu$.

The integration from the previous time is repeated with a step size to advance the solution to the time of slipping, the motion regime is changed, and the slipping equations are then advanced to the intended time with the displacement and velocities of the slab and walls at the time of slipping as the initial conditions. Marching then proceeds with the original time step.

If the slab was sliding on the wall at the last time step, the solution is advanced from τ_1 to τ_2 , say, integrating the equations of motion for the slipping regime, and the solution at $\tau = \tau_2$ is tested. If $|a(\tau_2)| > \mu$, marching proceeds to the next time step. If the $|a(\tau_2)| < \mu$ test succeeds, the difference test of the polynomials approximating the wall and slab velocities is performed. When the difference of velocities changes sign in the interval, the velocities being continuous in time must be equal somewhere in the interval. The time when the velocity difference is zero is calculated, and the integration of the slipping equations is advanced from the previous time to the time of sticking, time of zero velocity difference. The equations for sticking floor and walls are integrated from the time of sticking to τ_2 . Afterward, marching proceeds using the original step size.

Detail drawings of building plans¹² and photographs of construction underway¹³ shows that a reasonable floor slab bearing length is one half the wall thickness, $\delta = 1$. The difference in displacements, $\delta(\tau)$, is tested at each time step. Should the magnitude of the difference exceed 1, the assembly is considered to have collapsed, and the time at the present integration step is taken as the collapse time, τ_c . Since a structure which can resist a seismic loading for a shorter time before failing than another is more hazardous, a measure of the hazard is the collapse factor, a quantity proportional to $1/\tau_c$.

ACCELERATION FUNCTION

During an earthquake, the upper stories of a building are not subjected to an acceleration like those recorded by seismometers fixed to the ground. Instead, the exciting acceleration is a combination of the earthquake ground acceleration and the response of the lower floors. It could be said that the structure filters the earthquake acceleration, eliminating high frequency components and amplifying components that have frequencies near the fundamental frequency of the structure. This filtering is confirmed by examination of earthquake accelerograms¹⁴ recorded by instruments located in the basement and the top floor of structures, Fig. 24. The following analysis also suggests the result.

In a very simple way, a structure may be modeled as a linear one-degree-of-freedom oscillator with an "equivalent" mass, viscous friction, and stiffness. The motion of the oscillator is described by the following equation:

$$(6) \quad m \ddot{x} + c \dot{x} + k x = -m a(t)$$

where

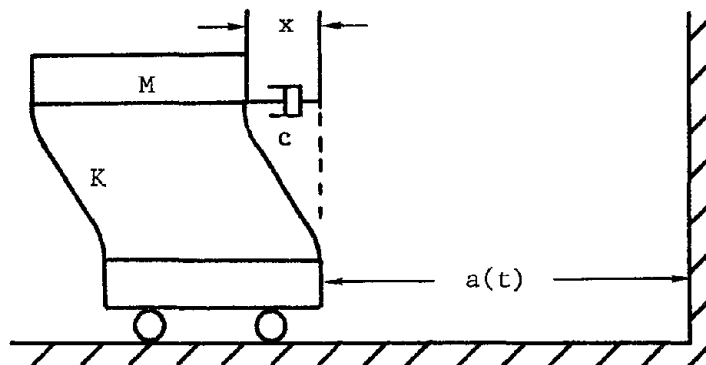
$x(t)$ = displacement from the undeformed position
relative to the base

m = equivalent mass

c = coefficient of viscous friction

k = equivalent stiffness

$a(t)$ = prescribed acceleration input



From the equilibrium equation, Equation (6), it is seen that it is the absolute acceleration of the mass, $\ddot{x} + a(t)$, that is related to the elastic and viscous reaction forces. Using available accelerograms of strong earthquake ground motion as input, the induced absolute acceleration, acceleration with respect to an inertial frame, of a one-degree-of-freedom linear oscillator was calculated; the Pacoima Dam Feb. 9, 1971 S14W component¹⁵ was used in this analysis. The discrete Fourier transform of the absolute acceleration of the oscillator and of the Pacoima Dam Feb. 9, 1971 S14W component itself was computed using the FFT algorithm¹⁶ on 512 evenly spaced data points over 10.22 seconds. The plots of the modulus of the Fourier coefficients versus frequency for both appear as Figure 25 and Figure 26. These figures show clearly that the spectral content of the linear oscillator absolute acceleration is much less complex. In fact, for the case shown, damping = 2% critical, undamped natural frequency = 1 Hz., the response of the absolute acceleration is composed for the most part of one frequency. Figure 27 shows the absolute value of the absolute acceleration versus time. A smooth envelope loosely corresponding the the acceleration peaks is superimposed. This motivates the choice of a sinusoidal oscillation contained within a smooth envelope as the acceleration function exciting the proposed shear wall-floor slab system.

The envelope function ($\exp (- \alpha t^* \tau) - \exp (- \beta t^* \tau))$) is a smooth, 2 parameter function which qualitatively describes the peaks of the response of a linear oscillator excited by an accelerogram input. Specifying τ_{rise} and τ_{dur} allows the parameters α and β to be evaluated. This was done for 3 pairs of τ_{rise} and τ_{dur} to yield 3 envelope functions with characteristics representative of a fast rising, a moderately rising, and a slowly rising envelope function as resulting from the response of a linear oscillator taking published fast rising, moderately rising, and slowly rising earthquake ground motion accelerograms as input. Table 4 shows the correspondence between the chosen nondimensional characteristic times and real time for a "8 inch" wall. Choosing

the acceleration function, $a(\tau)$, as

$$a(\tau) = \frac{2 g A (t^*)^2}{d S_{\max}} \left(\exp(-\alpha t^* \tau) - \exp(-\beta t^* \tau) \right) \sin \omega \tau$$

where

$$S_{\max} \equiv \max_{\tau > 0} \left\{ \left(\exp(-\alpha t^* \tau) - \exp(-\beta t^* \tau) \right) \sin \omega \tau \right\}$$

gives the oscillatory motion within an envelope of realistic proportion. The smooth envelope shown in Figure 27 is the moderately rising envelope.

RESULTS AND DISCUSSION

For each of the three envelope shapes, the collapse time is computed for amplitude A in the range of 0.7 A 1.15 and for frequency f in the range $0.5 \leq f \leq 1.125$, $f = \omega / 2\pi$. Because of the finite duration of earthquakes, the smaller collapse times represent greater hazard than the larger collapse times. The product of a scaling parameter, which is a reference nondimensional time, and the reciprocal of the nondimensional collapse time is called γ_c ; γ_c is plotted on the vertical scale of the cartesian coordinate system in reciprocal time-envelope amplitude-frequency space, in brief the γ - A - f space. The larger values of γ_c are the more significant. Computations were made with different scaling parameters to find a scaling parameter which makes the surfaces of γ_c in the γ - A - f space relatively independent of the envelope shape. Scaling parameters of τ_{rise} , τ_{max} , τ_{dur} , and 1 were tried. The greatest similarity is shown in the surfaces $\gamma_c(A, f) \equiv \tau_{\text{rise}} / \tau_c$ and $\gamma_c(A, f) \equiv \tau_{\text{max}} / \tau_c$; these surfaces are shown in Figs. 28 to 33. The cross-hatching in these figures represents lines parallel to the amplitude and frequency axes following the surface $\gamma_c(A, f)$. One notes that, for a given frequency, the collapse factor increases rapidly with amplitude after a critical amplitude is reached.

Figure 34 gives an indication of this steepness in the area of critical amplitude. On the other hand, the collapse factor γ_c decreases with increasing frequency at a fixed amplitude.

In addition, the complete displacement histories for certain A and f in the critical area were examined to demonstrate that the interval of integration was chosen adequately long to reach collapse in all possible cases. Figure 35 shows such a displacement record with the peak relative displacement $\delta(\tau)$ per cycle decreasing for $\tau > \tau_{\max}$. Such records also justify the use of the Coulomb friction model, as experiments¹¹ show that for concrete blocks sliding along cracked grouted and mortared surfaces, the friction ratio μ approaches the asymptotic Coulomb friction value after sliding about 0.4 inches. The present calculations show sliding of many times that distance before the collapse time is reached.

V PRACTICAL APPLICATION OF RESULTS FROM ONE-DEGREE-OF-FREEDOM
MODEL

There are two broad classes of mechanisms for structural system failure: the widespread structural member fracture, yield, and material overstressing failure and the kinetic instability failure where material failure is confined to connections only. A stress analysis can give the structural load carrying limits imposed by the building materials. The analysis in the last sections characterized the kinetic instability structural failure mode alternative. It will be shown later how a structure's conformance with the pertinent building code regulations can be assured.

The fundamental sections of the Uniform Building Code¹⁵ and the "Tentative Provisions for the Development of Seismic Regulations for Buildings" ATC 3-06¹⁶ impose what are essentially lower limits on the load carrying capacity of a structure. A conservative design practice necessitates finding out which of the failure modes outlined above is the "weakest link" for a particular building configuration then designing to meet or exceed the loading requirements imposed by the building codes. Both the UBC¹⁵ and ATC 3-06¹⁶ prescribe a static total lateral load to be reacted by the foundation of the structure and how that lateral load is to be distributed to the individual floors as a function of: expectation that the structure will be excited by an earthquake; construction materials; structural configuration; properties of the soil at the building site; the fundamental period and total weight of the structure. Comparing the resulting lateral force-vertical force ratios with the magnitude above which kinetic instability occurs for a particular structure shows which mode is the "weakest link".

As an illustration, a procedure for establishing which failure mode is the "weakest link" for an example structure, in conjunction with the UBC¹⁵ and ATC 3-06¹⁶ methodology, is

outlined below. Consider a sixteen story commercial office building to be built in Southern California (seismic zone #4). The configuration is to be a reinforced concrete frame with shear walls for additional stiffness. All the floors have the same weight, w , and the story height, Δh , is uniform. Assume that the floors are slabs set up on the frame with interface friction only causing the slab to move with the frame. The soil profile can be characterized by 30 feet or more of soft-medium-stiff clays with intervening layers of sand. In lieu of a dynamic analysis of the structure, use Equation 12-3A of section 2312 of the UBC¹⁵ to estimate the fundamental period of the structure.

$$(7) \quad T = \frac{0.05 h_n}{D}$$

T = fundamental period (seconds) in the direction parallel to the applied lateral forces

h_n = height of the structure having n floors in feet

D = dimension of structure, in feet, in a direction parallel to the applied forces

For convenience, take $h_n := 177$ and $D := 78.62$ giving the example structure realistic proportions and a fundamental period of 1 second. The above specifications allow the calculation of the minimum total lateral force to be reacted at the base and the distribution of lateral force to the individual floors according to the building codes by the following method (UBC¹⁵ pp.132-151).

$$(8) \quad V = ZIKCSW$$

where

V = total lateral force at the base

Z = earthquake zone coefficient

I = occupancy importance factor

K = structural configuration coefficient

C = fundamental frequency parameter
 S = site-structure resonance parameter
 W = total dead load (weight)

The UBC¹⁵ gives the following values for the example structure.

$Z = 1$ definitions sec. 2312 (b) p.134 UBC¹⁵
 $I = 1$ Table 23-K p.148 UBC¹⁵
 $K = 0.8$ Table 23-I p.146 UBC¹⁵
 $C = 0.06667$ by Equation (12-2) sec. 2312 UBC¹⁵
 $S = 1.5$ sec. 2312 (d) p.135 UBC¹⁵

Substituting into Equation (8) gives

$$(9) \quad V = 0.08 W.$$

Equation (12-5) sec. 2312 UBC¹⁵ gives the distribution of lateral force with height.

$$(10) \quad V = F_t + \sum_{i=1}^{16} F_i$$

where

F_i = lateral force applied to the i^{th} floor

F_t = an additional lateral force applied to the top floor

$$(11) \quad F_t = 0.07 T V \quad (\text{Equation (12-6) sec. 2312 UBC}^{15})$$

$$(12) \quad F_i \equiv (V - F_t) \frac{w_i h_i}{\sum_{j=1}^n w_j h_j} \quad (\text{Equation (12-7) sec. 2312 UBC}^{15})$$

h_i = height of i^{th} floor

w_i = weight of i^{th} floor

n = total number of floors

The F_i values are those lateral forces the building codes require a structure to carry without exceeding design allowables. In the case of the example structure, with $w_i = w$ and $h_i = i\Delta h$ and substituting Equation (11), Equation (12) simplifies to

$$(13) \quad F_i = 0.93 V \frac{i}{\sum_{j=1}^{16} j} = 0.93 V \frac{i}{136}$$

Because the load distribution is weighted with height, the top floor will receive the largest portion of the load and therefore will have the maximum lateral force-vertical force ratio.

Substituting Equation (9) into Equation (13) with $i := 16$, write the force ratio as follows:

$$(14) \quad \frac{F_{16}}{w} = \frac{0.93 V 16}{w 136} = \frac{0.93 (16^2) 0.08}{136} = 0.140$$

The ATC 3-06¹⁶ provides updated provisions which are applied in the same way as the UBC¹⁵ provisions. The calculation of the lateral force-vertical force ratio according to ATC 3-06¹⁶ follows. Similar to Equation (8), Equation (15) gives the total lateral force.

$$(15) \quad V \equiv C_s W$$

where C_s = seismic coefficient

$$C_s \equiv \frac{1.2 A_v S_{ATC3}}{R (T)^{2/3}}$$

A_v = effective peak velocity-related acceleration (sec. 1.4.1, p.28 ATC 3-06¹⁶)

S_{ATC3} = coefficient for the soil profile characteristic (Table 3-A, p.51 ATC 3-06¹⁶)

R = response modification factor (dependent on structural configuration and construction material)(Table 3-B, p.52 ATC 3-06¹⁶)

T = fundamental period of the structure in the direction parallel to the applied lateral forces (compute by Equation (7))

For the considered example structure, these coefficients take these values:

$$\begin{aligned} A_V &= 0.4 \\ S_{ATC3} &= 1.5 \\ R &= 5.5 \\ T &= 1 \end{aligned}$$

For these,

$$(16) \quad C_s = 0.13091.$$

The force distribution is given by Equation (17).

$$(17) \quad F_i = C_{vi} V \quad (\text{Equation 4-6, p.57, ATC 3-06}^{16})$$

where

$$(18) \quad C_{vi} \equiv \frac{w_i h_i^k}{\sum_{j=1}^n w_j h_j^k} \quad (\text{Equation 4-6a, p.57, ATC 3-06}^{16})$$

The value of the exponent, k , is given on page 56, ATC 3-06¹⁶.

For a structure with a fundamental period of 1 second, $k = 1.25$.

As before, make the simplifying assumptions, $w_i = w$, $i = 1, 16$ and

$h_i = i\Delta h$ so that Equation (18) becomes

$$(19) \quad C = \frac{i^{1.25}}{\sum_{j=1}^{16} (j)^{1.25}}.$$

Again, because of the weighted lateral force distribution, the greatest lateral force-vertical force ratio will occur at the top floor. Taking $i := 16$, Equation (19) becomes

$$(20) \quad C_{v16} = \frac{32}{243.7150} = 0.131301.$$

Divide Equation (17) by w , substituting Equations (15), (16), and (20), find that

$$(21) \quad \frac{F_{16}}{w} = C_{v16} C_s 16 = 0.131301 (0.13091) 16 = 0.275 .$$

The lateral force-vertical force ratio above which kinetic instability becomes important can be found by inspection from the results of the previous analysis of the kinetic stability of the prototype one-degree-of-freedom structure. For the example structure, the fundamental frequency is 1 Hz. and the soil profile suggests that an earthquake would have a moderately rising acceleration envelope. Therefore, consider the γ -A-f surface of Fig. 29. For $f = 1$ Hz., find the largest A for which $\gamma_c = 0$, the largest A in the safe zone. This A is found to be

$$(22) \quad A = 0.95g \Rightarrow \frac{F_{16}}{w} = 0.95$$

The critical lateral force-vertical force ratio above which failure by kinetic instability will occur is 0.95.

The results, Equations (14), (21), and (22) allow failure mode and code compliance evaluation. While the results for the UBC¹⁵, Equation (14), and from ATC 3-06¹⁶, Equation (21), prescribe lower bounds on the lateral load carrying capacity of a structure and not the design allowable loading, a simple beam bending analysis of a real building (Urey Hall on the U.C., San Diego campus) suggests that structures are designed to meet the code requirements for lateral loading with little reserve. It is therefore realistic to take the lower bound given by the building codes as the load above which the structure will fail. It is seen that the load carrying requirements from the UBC¹⁵, $F_{16} = 0.140 w$, and from ATC 3-06¹⁶, $F_{16} = 0.275 w$, are significantly less than the $F_{16} \geq 0.95 w$ required to initiate kinetic instability. One concludes from this that the example structure will suffer a structural fracture, yield and material overstress type failure before any kinetic instability could occur.

There is some feeling among structural analysts that the updated and more stringent requirements of ATC 3-06¹⁶ may not be sufficient and that further increases in lateral load carrying capacity are necessary for conservative design. Should more stringent requirements be adopted in the future, that a structure would fail by structural member overstressing instead of by kinetic instability would not be so clear as it was in the above example, and the kinetic stability of the structure ought to be verified. This would be especially true for structures with longer fundamental periods since the trend of the kinetic stability result indicates increased hazard for increased fundamental periods, and the tentative result of the more sophisticated model discussed in the next section suggests that the consideration of vertical seismic acceleration causes the critical zone for kinetic instability to occur at lower lateral acceleration amplitudes.

VI TWO-DEGREE-OF-FREEDOM MODEL ALLOWING PLANAR MOTION OF
FLOOR SLAB

While the simple one-degree-of-freedom model of the last section is considered adequate to demonstrate certain trends in the behavior of masonry structures, and to show that the numerical techniques developed to handle the Coulomb friction condition are capable of producing practical results, it ignored for the sake of simplicity some features of earthquake ground motion and more general structural response. The principal new features to be considered in this section are the description of the planar motion of the slab and the accommodation of the influence of the vertical component of ground acceleration. Since accelerogram records show that the orthogonal horizontal components of ground acceleration have comparable peak magnitudes (References 14 and 15), then admission of planar motion of the slab is an important generalization of the model. Since the horizontal frictional forces are assumed in the model to be directly proportional to the vertical acceleration of the slab while sliding, then the effect of the vertical component of acceleration on the horizontal slab motion is significant. These features are incorporated in this section into a more general shear-wall floor slab model than is considered in chapters IV and V.

Consider a rigid floor slab resting on directly opposing, rigid, parallel shear-walls built into a rigid base similar to the configuration of Fig. 23 studied in the last sections. Again, the floor slab is constrained to move with the shear-walls by Coulomb friction with a constant coefficient acting between adjacent floor slab and shear-wall surfaces. Displacements of the floor slab parallel and perpendicular to the shear walls are allowed, Figs. 36a and 36b. Rotations of the base or slab are not considered. While vertical components of velocities and displacements of the

slab relative to the shear walls are assumed to be zero, the effect of a prescribed vertical acceleration of the shear-walls is considered in calculating the Coulomb frictional force acting between floor slab and shear-wall. These assumptions are considered adequate for the heavy floor slabs used in practice and for reasonable magnitudes of vertical acceleration, and they greatly simplify the analysis.

Define the following variables:

$x_s(\tau) \equiv$ dimensionless horizontal displacement of slab perpendicular to the plane of the walls from its $\tau = 0$ location

$x_b(\tau) \equiv$ dimensionless horizontal displacement of the base perpendicular to the plane of the walls from its $\tau = 0$ location

$y_s(\tau) \equiv$ dimensionless horizontal displacement of slab parallel to the plane of the walls from its $\tau = 0$ location

$y_b(\tau) \equiv$ dimensionless horizontal displacement of the base parallel to the plane of the walls from its $\tau = 0$ location

$a_x(\tau) \equiv$ prescribed dimensionless horizontal acceleration of base perpendicular to the plane of the walls

$a_y(\tau) \equiv$ prescribed dimensionless horizontal acceleration of base parallel to the plane of the walls

$a_v(\tau) \equiv$ prescribed dimensionless vertical acceleration of the assemblage in the up direction

Note that $x_s(\tau)$, $y_s(\tau)$, $x_b(\tau)$, and $y_b(\tau)$ are measured relative to their $\tau = 0$ values from a nonrotating inertial frame fixed in space. The describing equations of motion for the sticking and slipping regimes, conditions of regime change, and initial conditions follow:

$$x_s(\tau) = \dot{x}_s(\tau) = x_b(\tau) = \dot{x}_b(\tau) = y_s(\tau) = \dot{y}_s(\tau) = y_b(\tau) = \dot{y}_b(\tau) \\ \text{at } \tau = 0$$

If the floor slab is sticking to the walls,

$$\begin{aligned}\ddot{x}_s(\tau) &= a_x(\tau) \\ \ddot{x}_b(\tau) &= a_x(\tau) \\ \ddot{y}_s(\tau) &= a_y(\tau) \\ \ddot{y}_b(\tau) &= a_y(\tau)\end{aligned}$$

The floor slab will begin sliding if

$$((a_x(\tau))^2 + (a_y(\tau))^2)^{1/2} > -\mu a_v(\tau)$$

If the floor slab is sliding on the walls,

$$\begin{aligned}\ddot{x}_s(\tau) &= -\mu a_v(\tau) (\dot{x}_s(\tau) - \dot{x}_b(\tau)) / ((\dot{x}_s(\tau) - \dot{x}_b(\tau))^2 + (\dot{y}_s(\tau) - \dot{y}_b(\tau))^2)^{1/2} \\ \ddot{x}_b(\tau) &= a_x(\tau) \\ \ddot{y}_s(\tau) &= -\mu a_v(\tau) (\dot{y}_s(\tau) - \dot{y}_b(\tau)) / ((\dot{x}_s(\tau) - \dot{x}_b(\tau))^2 + (\dot{y}_s(\tau) - \dot{y}_b(\tau))^2)^{1/2} \\ \ddot{y}_b(\tau) &= a_y(\tau)\end{aligned}$$

The floor slab will stop sliding if three conditions hold, viz.

$$-\mu a_v(\tau) > ((a_x(\tau))^2 + (a_y(\tau))^2)^{1/2}, \dot{x}_s(\tau) = \dot{x}_b(\tau), \text{ and } \dot{y}_s(\tau) = \dot{y}_b(\tau)$$

The numerical results for the planar model were generated with code written in logical divisions similar to those used in the code for the one-degree-of-freedom model. For the sake of simplicity and economy, the code for the planar model interpolates linearly to approximate quantities between integration points. The planar model formulation has been demonstrated to be a consistent generalization of the one-degree-of-freedom case by calculating results with the planar model code for the special case $a_v(\tau) = -1$, $y_s(\tau) = y_b(\tau) = 0$ which is equivalent to the one-degree-of-freedom case. The results so calculated are in agreement with those calculated using the one-degree-of-freedom formulation.

The prescribed horizontal acceleration functions were again taken to be of the following form:

$$a_x(\tau) = \frac{2 g A_x (t^*)^2}{d S_{\max}} \left(\exp(-\alpha t^* \tau) - \exp(-\beta t^* \tau) \right) \sin \omega_x \tau$$

$$a_y(\tau) = \frac{2 g A_y (t^*)^2}{d S_{\max}} \left(\exp(-\alpha t^* \tau) - \exp(-\beta t^* \tau) \right) \sin \omega_y \tau$$

$$S_{\max} \equiv \max_{\tau > 0} \left(\exp(-\alpha t^* \tau) - \exp(-\beta t^* \tau) \right)$$

Acceleration functions of this form simulate the earthquake response of the upper floors of a lightly damped elastic structure. If $|x_s(\tau) - x_b(\tau)| > 1$ or $|y_s(\tau) - y_b(\tau)| > \theta$, the assemblage becomes unstable since the slab has moved off its supporting walls and is considered to have failed.

$$\theta \equiv 2 \text{ (wall length) } / \text{ (wall width)}$$

The value of $\theta := 20$ was used for all of the numerical experiments. The failure condition $|y_s(\tau) - y_b(\tau)| > \theta$ did not occur for any of the cases studied. The stability calculation was performed for a practical range of prescribed ω_x and ω_y :

$$f_x = \omega_x / 2 \pi t^* := 0.5, 0.625, 0.75, 0.875, 1.0, 1.125, 1.25, \\ 1.5, 2.0 \text{ Hz.}$$

$$f = \omega / 2 \pi t^* := 0.2, 0.5, 1.0, 2.0, 5.0, 10.0 \text{ Hz.}$$

This is a range of frequencies somewhat wider than that used in the one-degree-of-freedom calculation. The values of α and β giving the moderately rising envelope were used. The values of A_x were

taken to be

$$A_x := 0.5, 0.55, 0.6, 0.65, 0.7, 0.75, 0.8, 0.85, 0.9, \\ 0.95, 1.0, 1.05, 1.1, 1.15$$

A_y was chosen so that $A_y = 0.9 A_x$ since the approximate ratio of maximum horizontal acceleration components taken from the Pacoima Dam accelerogram was 0.9. The dimensionless sum of the vertical component of the Pacoime Dam accelerogram and gravity was used in all cases as the dimensionless prescribed vertical acceleration of the assemblage in computing the effective frictional force acting on the floor slab. The stability calculation was repeated six times. In computing each resulting surface, a different constant ω_y was selected while ω_x and A_x were allowed to range through their possible values. This progression of surfaces illustrates the trends in the failure surfaces with changes in the frequency of the acceleration component in the direction parallel to the walls. Figures 37-42 show the $\gamma_c - A_x - f_x$ surfaces resulting from the calculation. Note that while the plotting routines used to produce these figures uses linear interpolation in drawing the net, it is the points representing the computed results that are significant; the interconnecting lines serve to delineate the surface. The result of the one-degree-of-freedom model showed that as the frequency of excitation increased the amplitude of excitation must also be increased to cause the assemblage to fail. This trend generally extends to the planar model as well. As the constant underlying frequency, ω_y , increases, the amplitude of acceleration necessary to cause failure increases.

One sees that the critical zones from the result of the two-degree-of-freedom model occur at lower lateral accelerations than do the critical zone results from the one-degree-of-freedom model. The result of a true planar slab motion model, including two linear degrees-of-freedom and a rotational degree-of-freedom, could show further reduction in critical lateral acceleration, therefore increased hazard from kinetic instability. In which case, the verification of a structure's kinetic stability would be warranted, especially if building codes are revised to require increased lateral load carrying capacity, since the inertial loads on the slab could be large enough to cause slab sliding and yet be less than a structure's design allowable lateral load.

REFERENCES

- 1 Den Hartog, J.P., Mechanical Vibrations, McGraw-Hill, New York, 1947
- 2 Ziegler, H., Principles of Structural Stability, Blaisdell, Waltham, Massachusetts, 1968
- 3 Frazer, R.A., W.J. Duncan, A.R. Collar, Elementary Matrices and Some Applications to Dynamics and Differential Equations, Cambridge University Press, London, 1960
- 4 Kirkpatrick, P., "Seismic Measurements by the Overthrow of Columns", Bull. Seism. Soc. Am., V 17, # 2, 1927, pp. 95-109
- 5 Photographs courtesy of Prof. G. Krishnamoorthy
- 6 Housner, G.W., P.C. Jennings, A.G. Brady, "Earthquake Effects on Special Structures", P.C. Jennings, ed., Engineering Features of the San Fernando Earthquake February 9, 1971, Earthquake Engineering Research Laboratory, EERL 71-02, California Institute of Technology, Pasadena, California, 1971
- 7 Frazier, G.A., J.H. Wood, G.W. Housner, "Earthquake Damage to Buildings", P.C. Jennings, ed., Engineering Features of the San Fernando Earthquake February 9, 1971, EERL 71-02, California Institute of Technology, Pasadena, California, 1971
- 8 Noland, J.L., ed., Proceedings of the North American Masonry Conference, University of Colorado, Boulder, Colorado, August 1978
- 9 Hegemier, G.A., S.K. Arya, G. Krichnamoorthy, W. Nachbar, R. Furgerson, "On the Behavior of Joints in Concrete Masonry", J.L. Noland, ed., Proceedings of the North American Masonry Conference, August 1978, University of Colorado, Boulder, Colorado
- 10 Brownlee, K.A., Statistical Theory and Methodology In Science and Engineering, Wiley, New York, 1965
- 11 Nachbar, W., R. Furgerson, "Statistical Analysis of Post-Fractured Concrete Masonry Joints", Report AMES-NSF TR-76-8 University of California, San Diego, 1976

- 12 Amrhein, J.E., Reinforced Masonry Engineering Handbook ,
Masonry Institute of America, Los Angeles, California, 1972
- 13 Johnson, F.B., ed., Designing, Engineering, and Constructing
with Masonry Products , Proceedings of the International
Conference of Masonry Structural Systems, University of Texas at
Austin, Austin, Texas, 1969
- 14 "Strong Motion Earthquake Accelerograms: Digitized and Plotted
Data", Vol. I - Uncorrected Accelerograms, Part S - Accelerograms
IS255 - IS273, Report # EERL 73-24, Earthquake Engineering
Research Laboratory, California Institute of Technology,
Pasadena, California, October 1974
- 15 "Strong Motion Earthquake Accelerograms: Digitized and Plotted
Data", Vol. II - Corrected Accelerograms and Integrated
Ground Velocity and Displacement Curves, Part C, Report # EERL
72-51 PB - 220 162, Earthquake Engineering Research Laboratory,
California Institute of Technology, Pasadena, California
- 16 Ahmed, N., K.R. Rao, Orthogonal Transformations for Digital
Signal Processing , Springer-Verlag, Berlin, 1975
- 17 Uniform Building Code , International Conference of Building
Officials, Whittier, California, 1976
- 18 Tentative Provisions for the Development of Seismic Regulations
for Buildings; a Cooperative Effort with the Design Professions,
Building Code Interests and the Research Community , Applied
Technology Council Associated with the Structural Engineers
Association of California, Applied Technology Council Publication
ATC 3-06, National Bureau of Standards Special Publication 510,
National Science Foundation Publication 78-8, June 1978

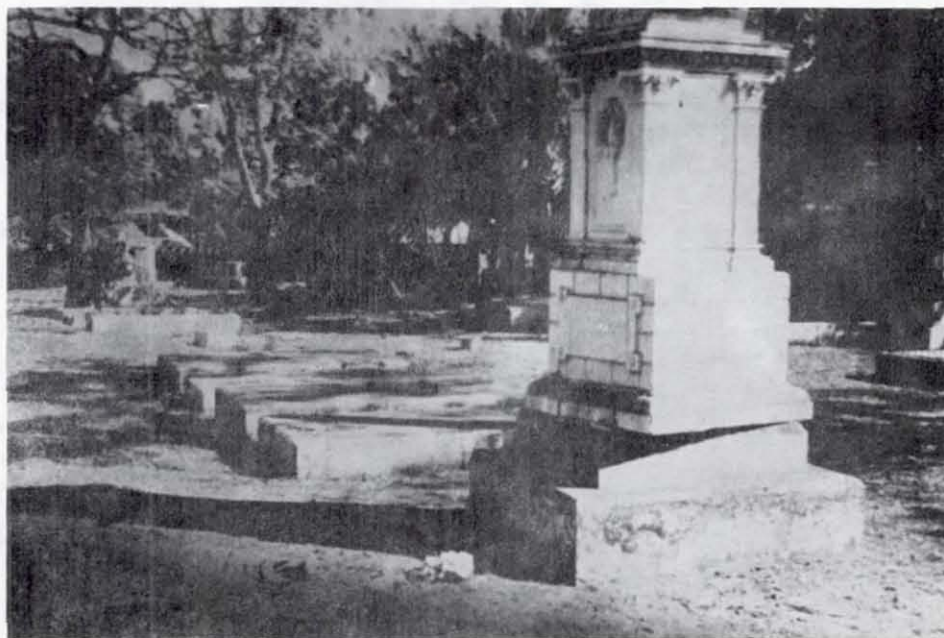


Figure 1 A monument, rotated on its base, after the Managua, Nicaragua earthquake, December 23, 1972.⁵

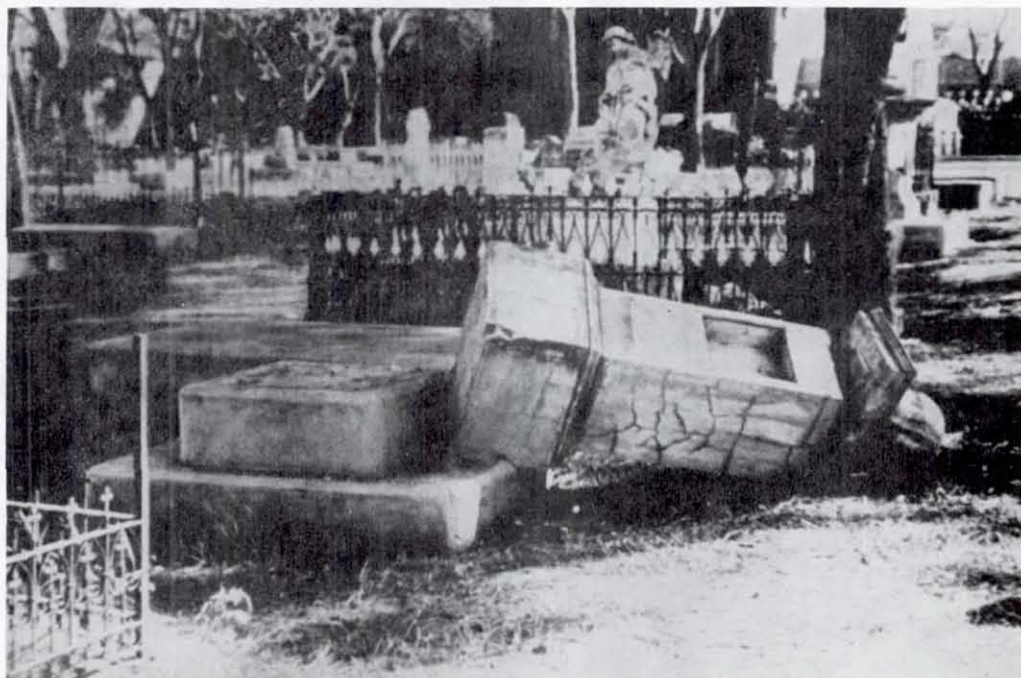


Figure 2 A toppled monument after the Managua, Nicaragua earthquake, December 23, 1972.⁵

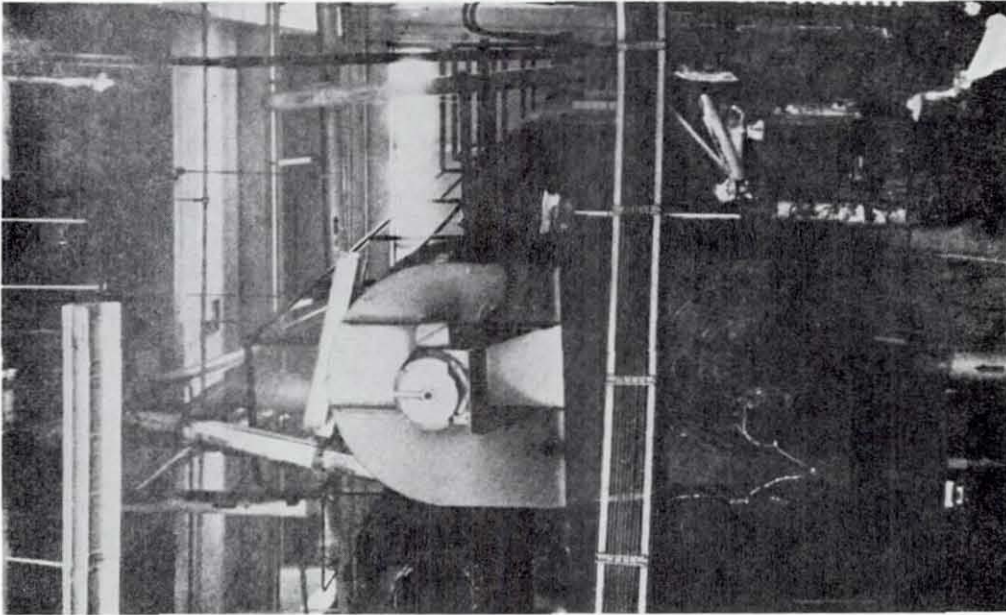


Figure 3 The boiler room of the Olive View Hospital after the San Fernando earthquake of February 9, 1971. The angle of the plumbing attached to the boiler, vertical before the earthquake, gives an indication of the sliding that took place.⁶

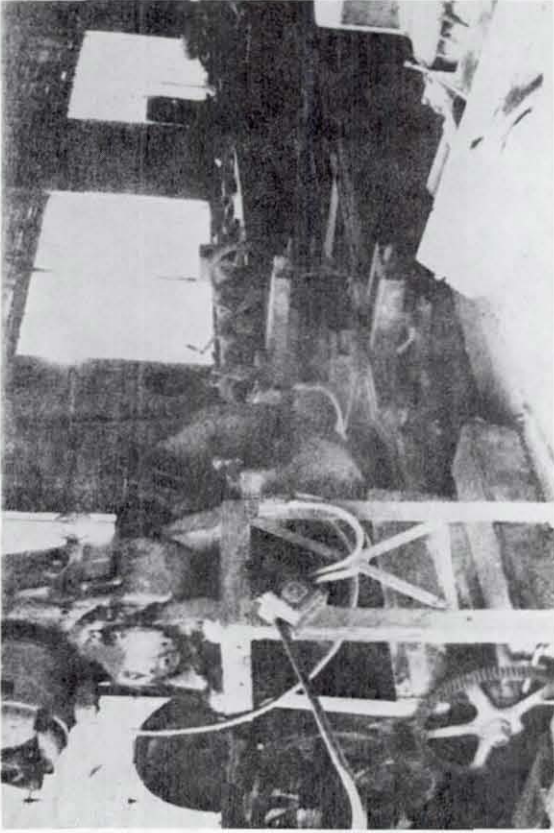


Figure 4 Skid marks showed that this heavy lathe slid 9 feet across the machine shop floor during the San Fernando earthquake, February 9, 1971.⁶

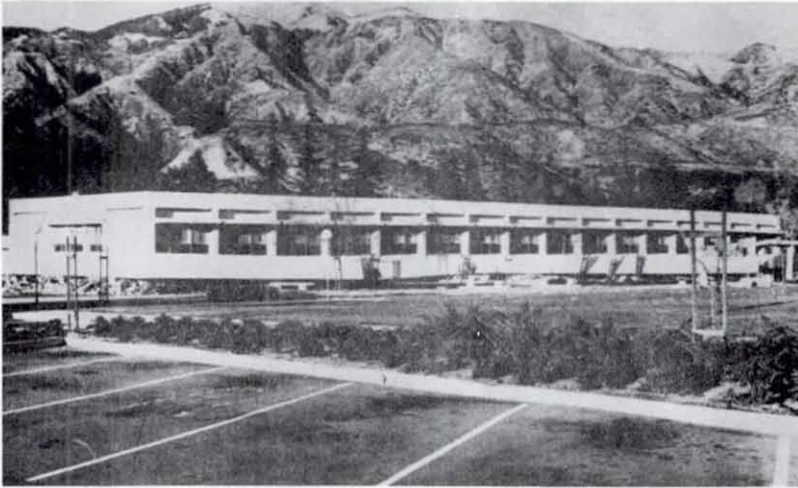


Figure 5 The first floor of the Psychiatric Day Care Center collapsed, the second floor is shown intact. Olive View Hospital after the San Fernando earthquake, February 9, 1971.⁷

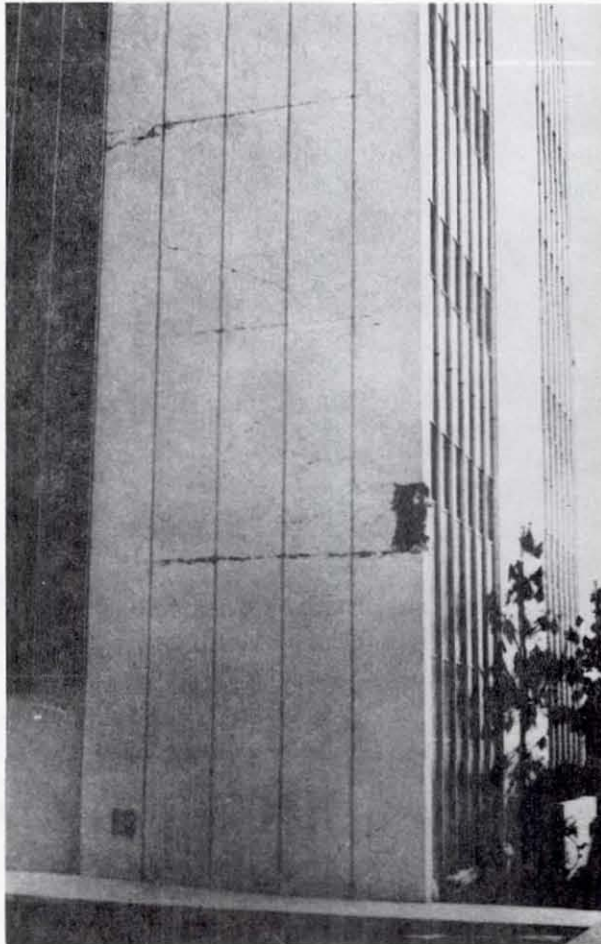


Figure 6 A shear wall in a multi-story building shows displacements at construction joints after the San Fernando earthquake, February 9, 1971.⁷

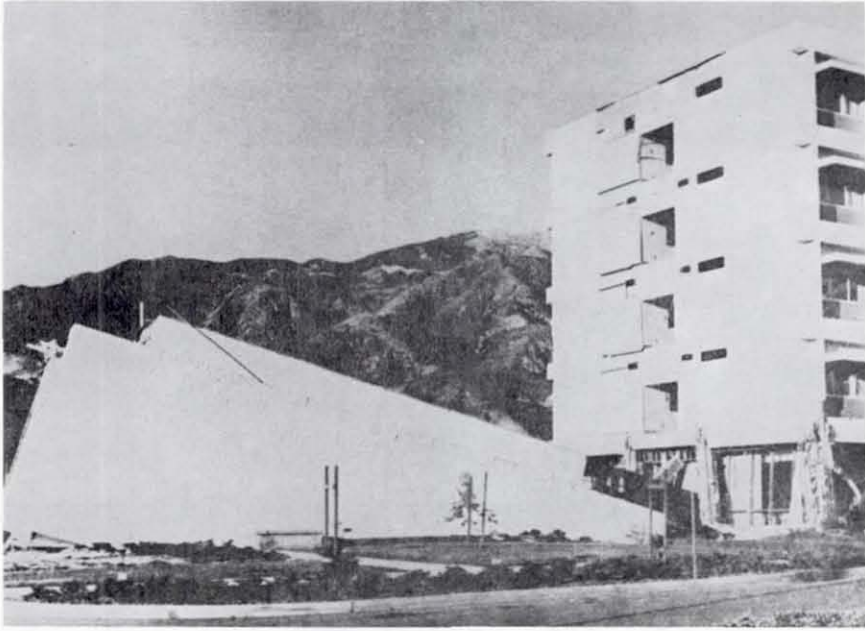


Figure 7 An intact stairwell has toppled at the Olive View Hospital after the San Fernando earthquake, February 9, 1971.⁷



Figure 8 The penthouse of this hotel rotated during the Managua, Nicaragua earthquake, December 23, 1972.⁵

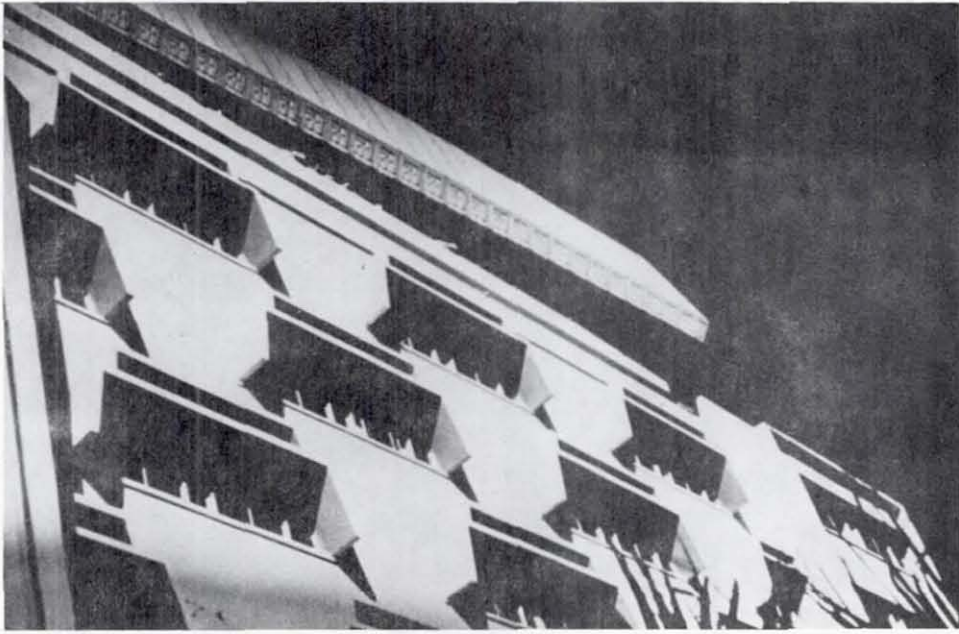


Figure 9 The same penthouse as in Figure 8 viewed from a different angle.⁵

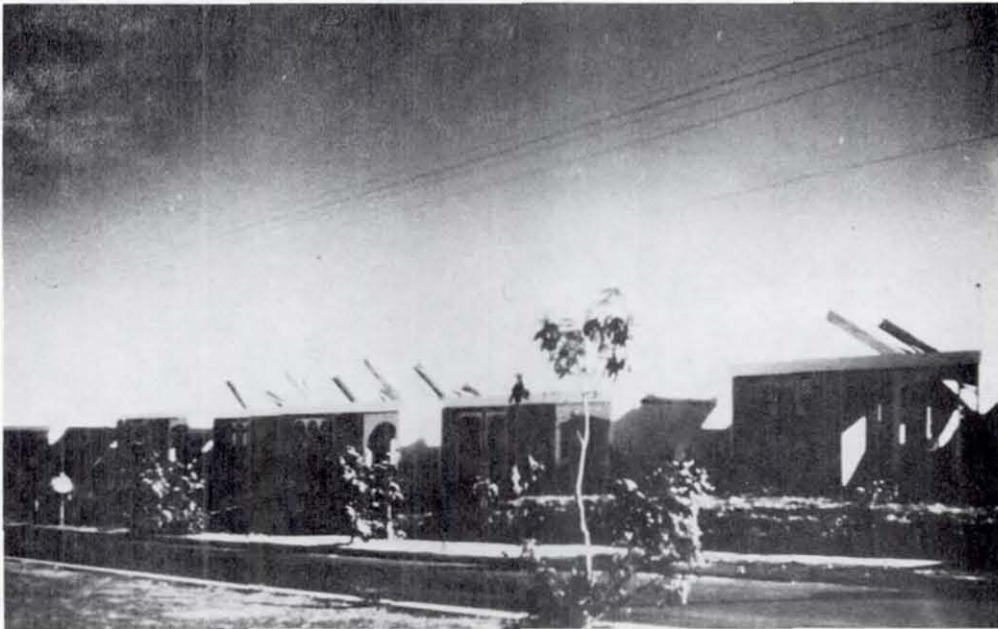


Figure 10 The roof channels of the homes in this tract slipped off their supporting walls in similar ways during the Managua, Nicaragua earthquake, December 23, 1972.⁵

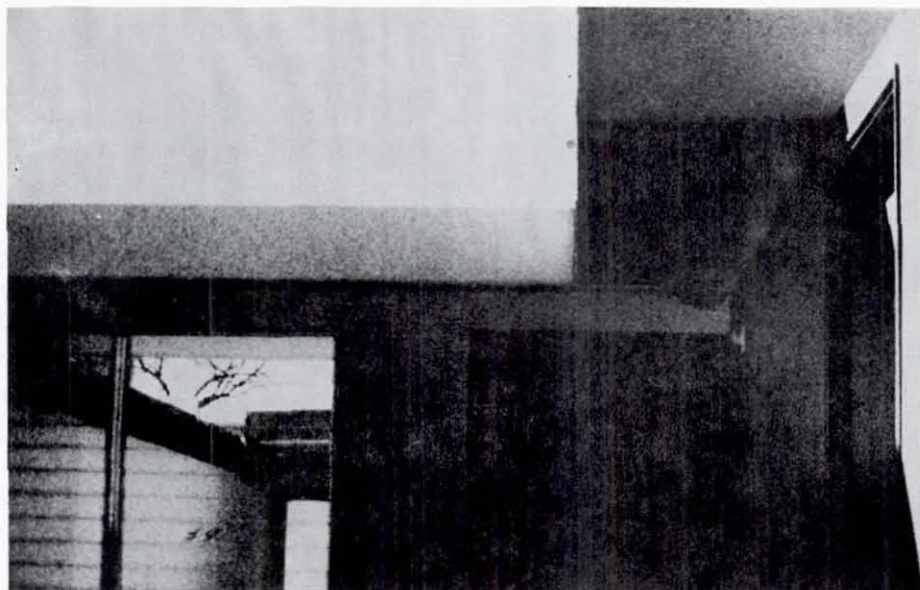
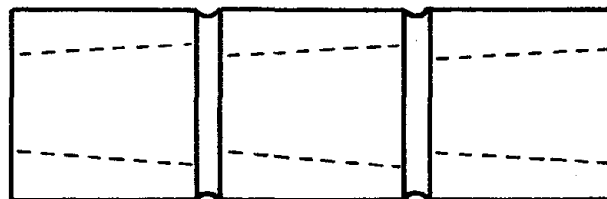
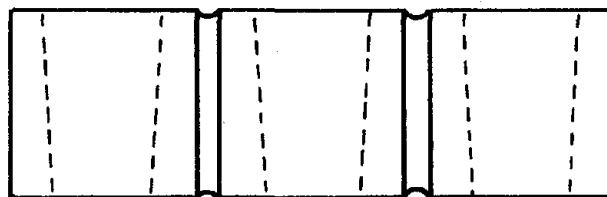


Figure 11 The roof channel of this home slipped some inches to the left during the Managua, Nicaragua earthquake, December 23, 1972. The dark area on the underside of the roof channel formerly bore on the supporting wall, the light area is the ceiling paint of the room through the door to the right.⁵



Bed Joint Triplet



Head Joint Triplet

Figure 12

Orientation of the block hollows for the bed joint and the head joint.

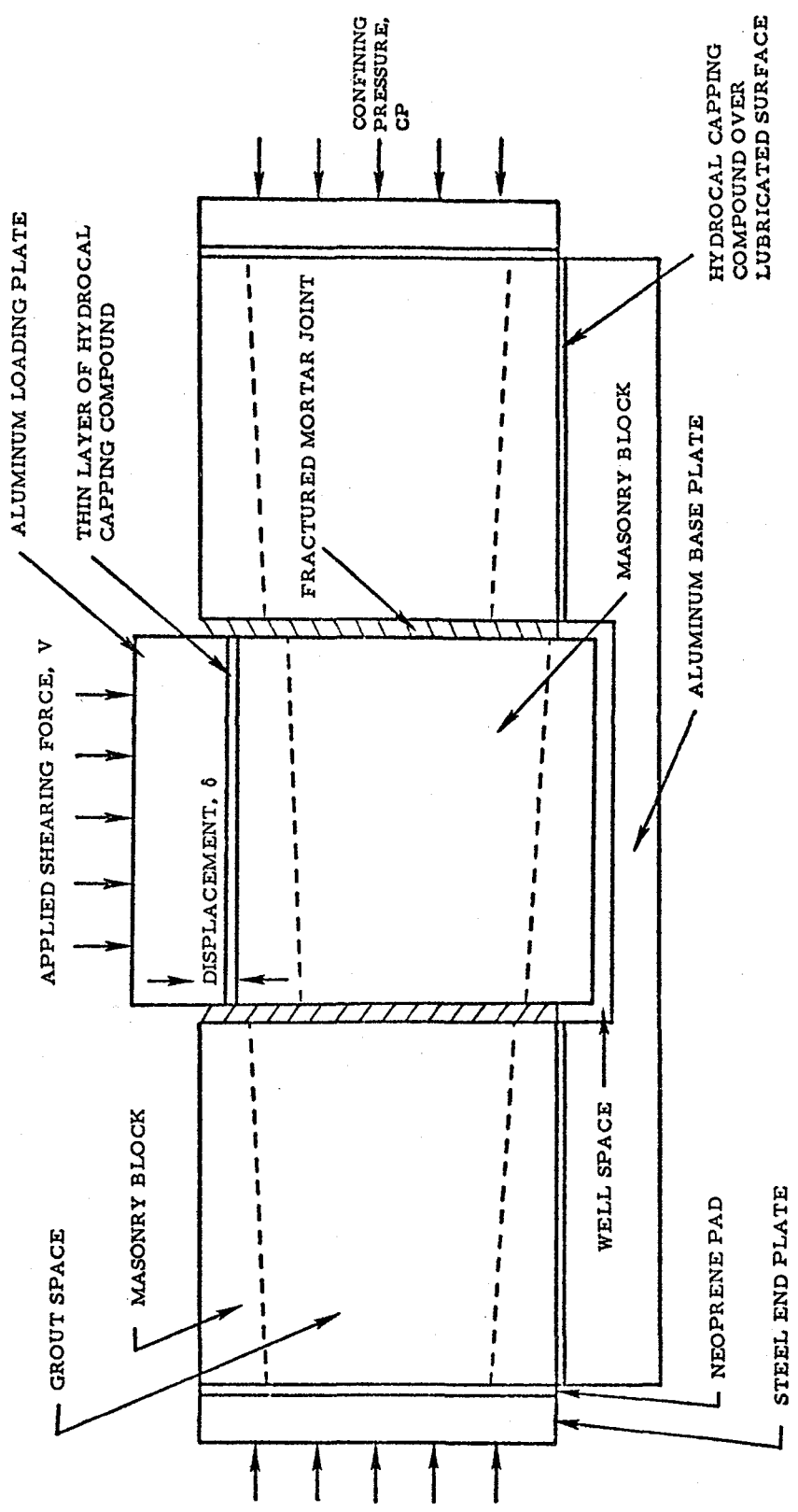


Figure 13 Concrete masonry half-block triplet in static shear test after joint fracture. (Bed joint illustrated, displacement exaggerated).

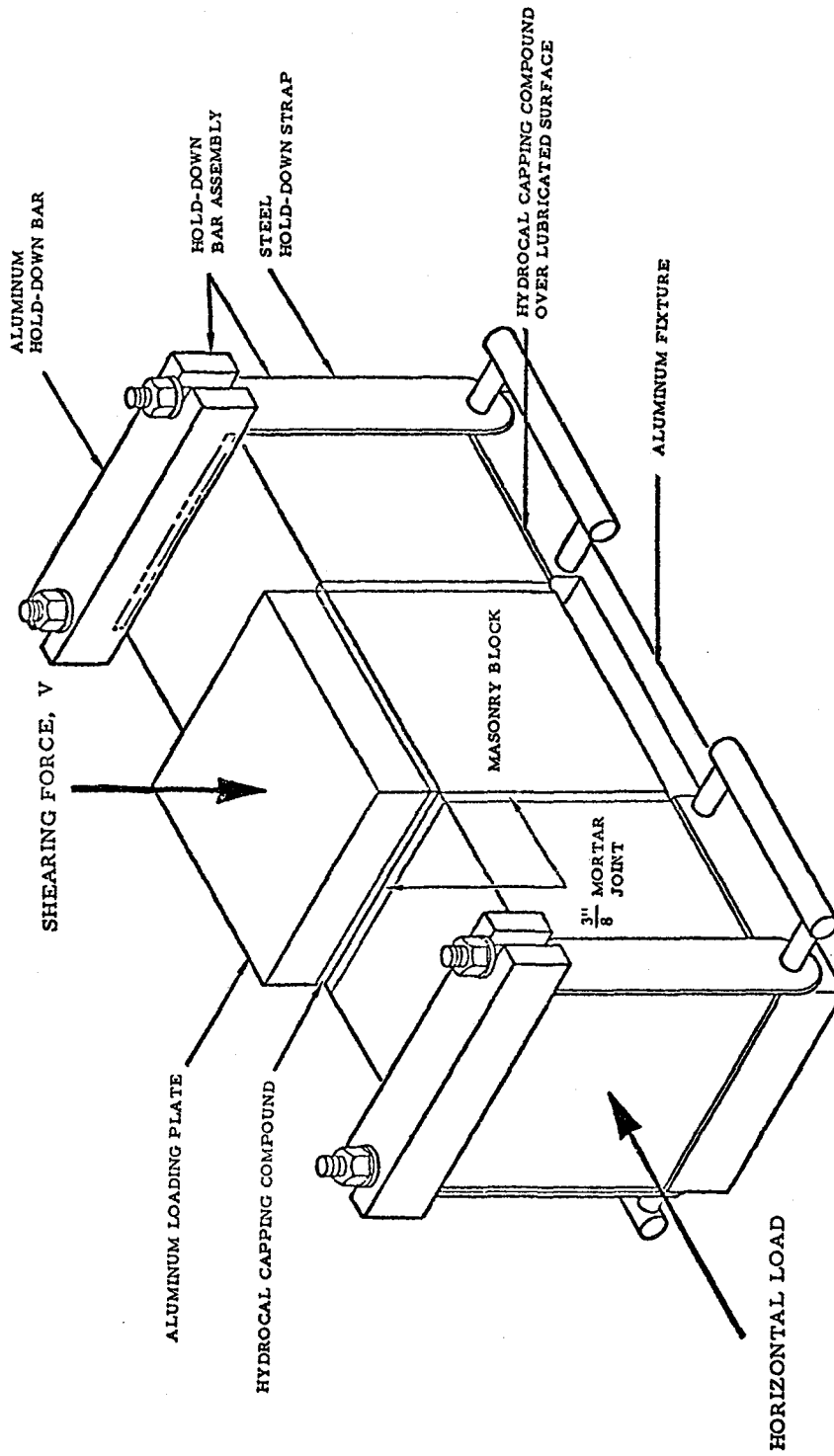


Figure 14 Concrete masonry half-block (7 5/8" x 7 5/8" x 7 5/8") triplet in static shear test. A perspective of the undeformed specimen in fixture.

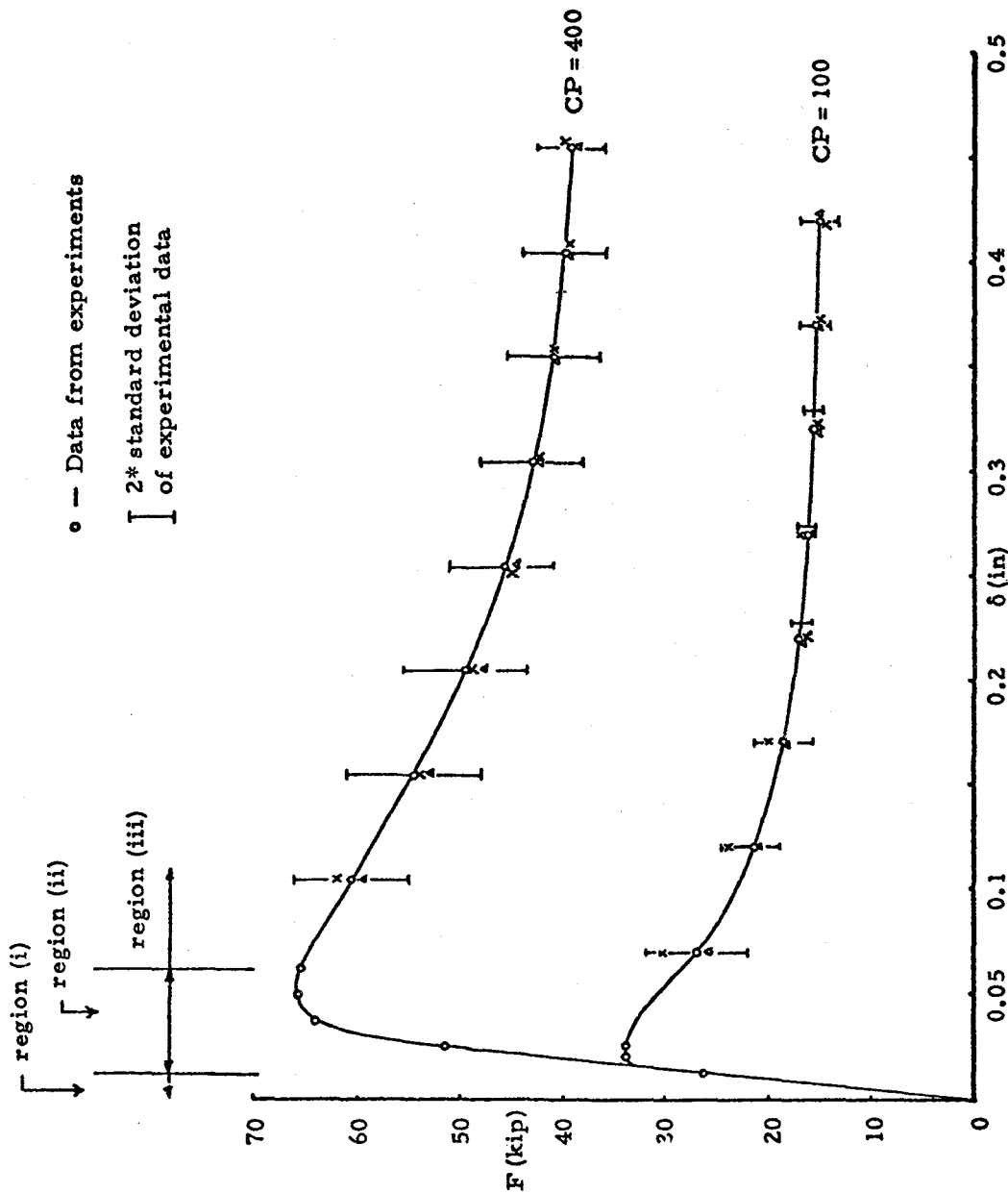


Figure 15 Typical experimental curves of total shear load V vs. deflection δ ; δ is measured from unloaded state. (Data points are sample mean values of V at each δ ; the half-height of the vertical bar equals the unbiased estimate of the standard deviation for the sample. In each case, sample size was 3 runs.)

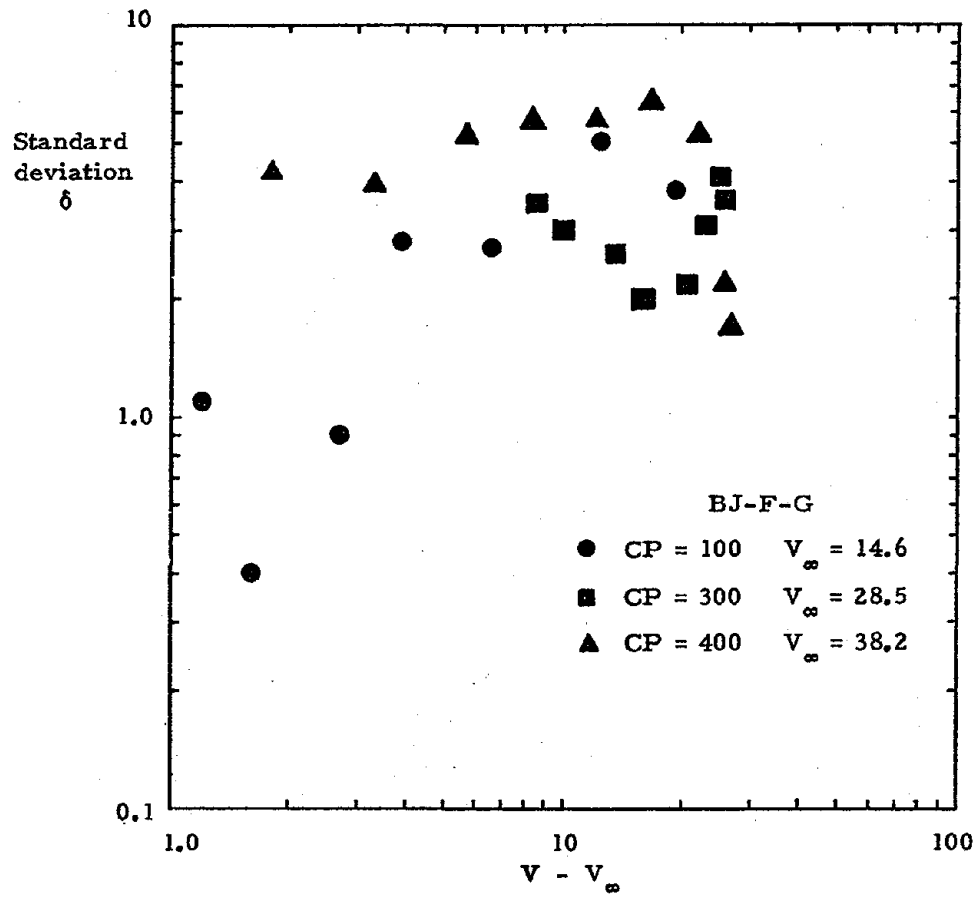


Figure 16

Variation of standard deviation vs. sample mean for several different tests.

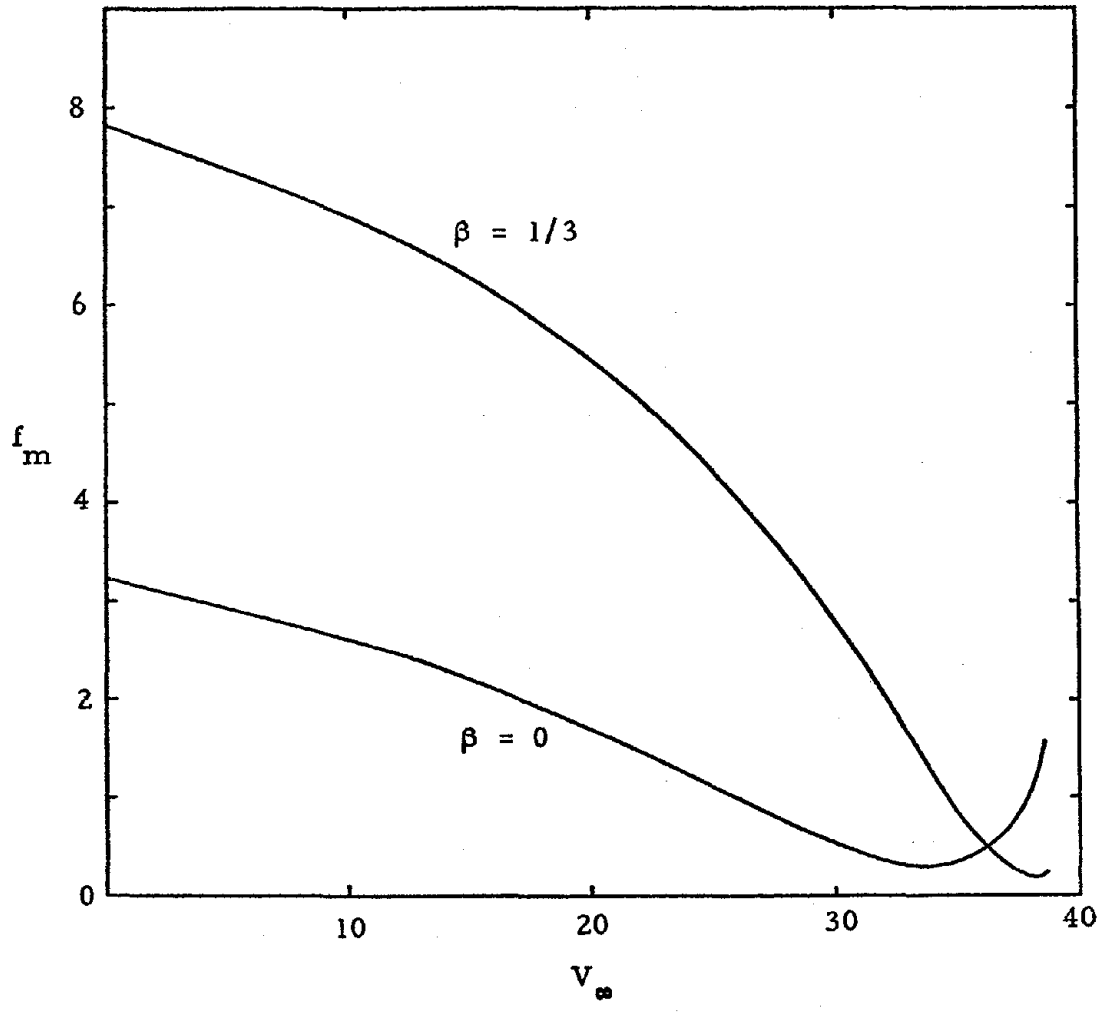


Figure 17

Minimization of f_m as function of V_∞ in a typical case (BJ-F-G-400) with $\alpha = 2$, and two values of β .

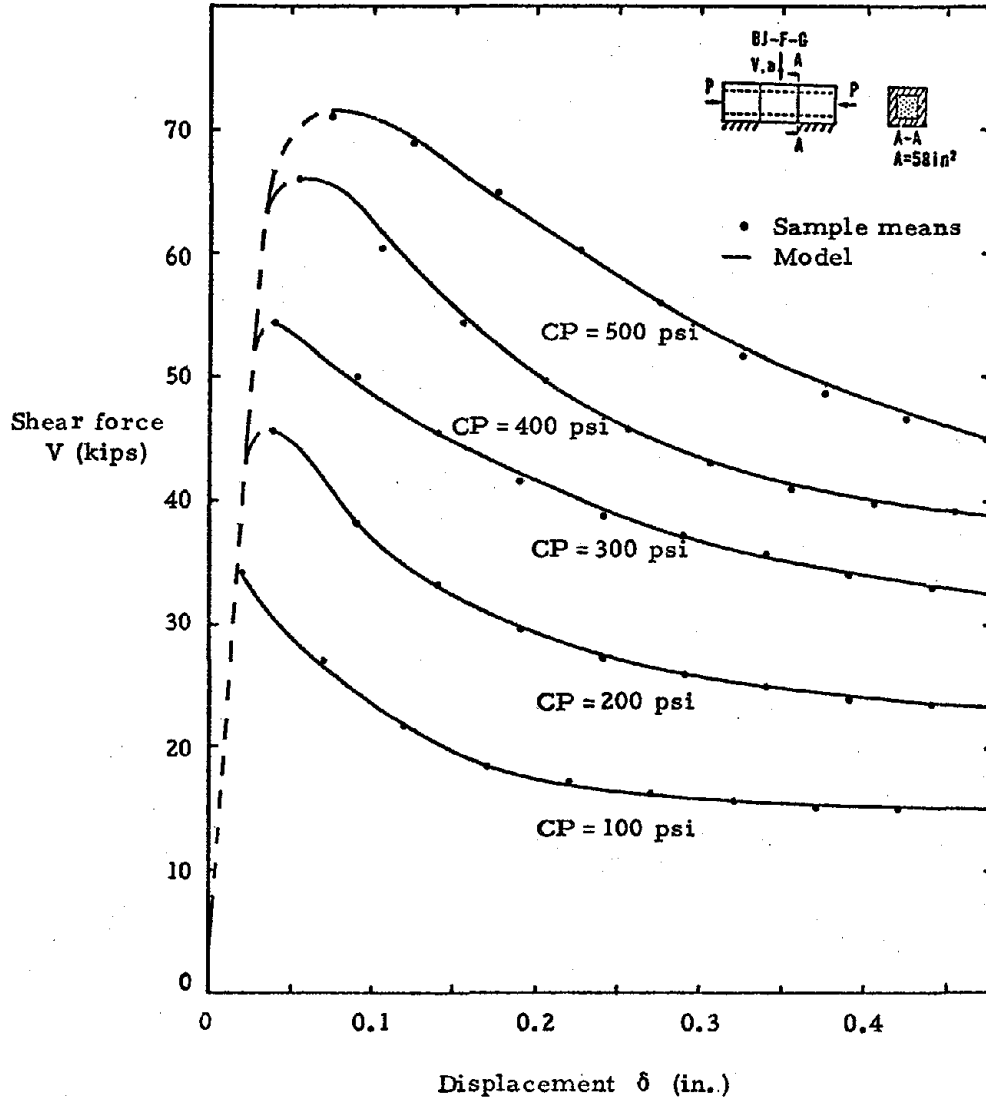


Figure 18

Comparison of model with experiment for the fully-grouted bed joints.

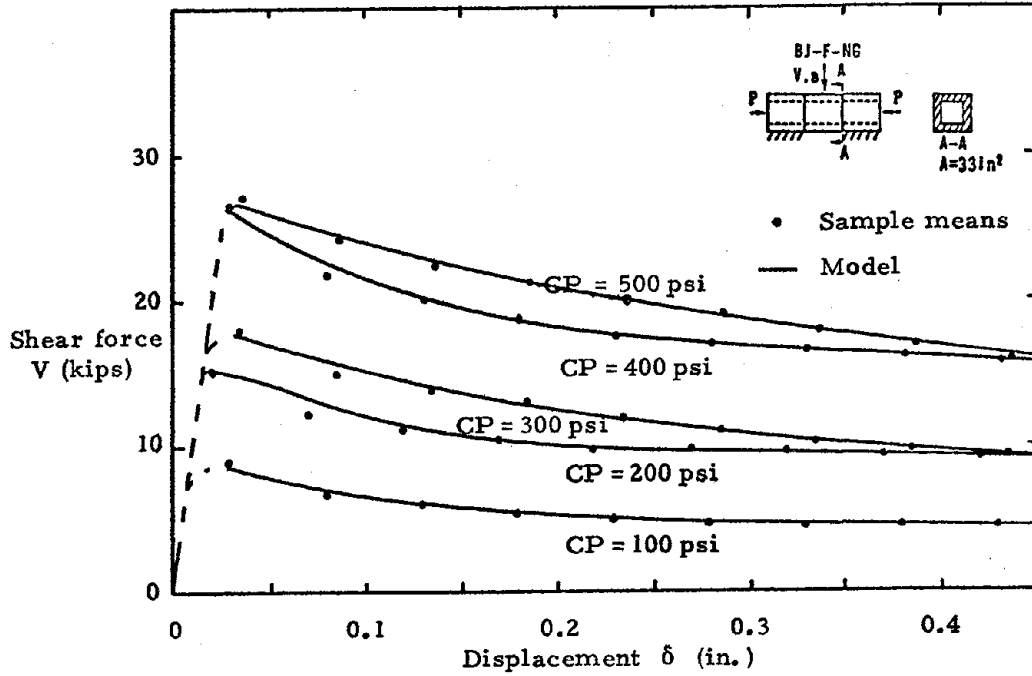


Figure 19 Comparison of model with experiment for the ungrouted bed joint (mortar only).

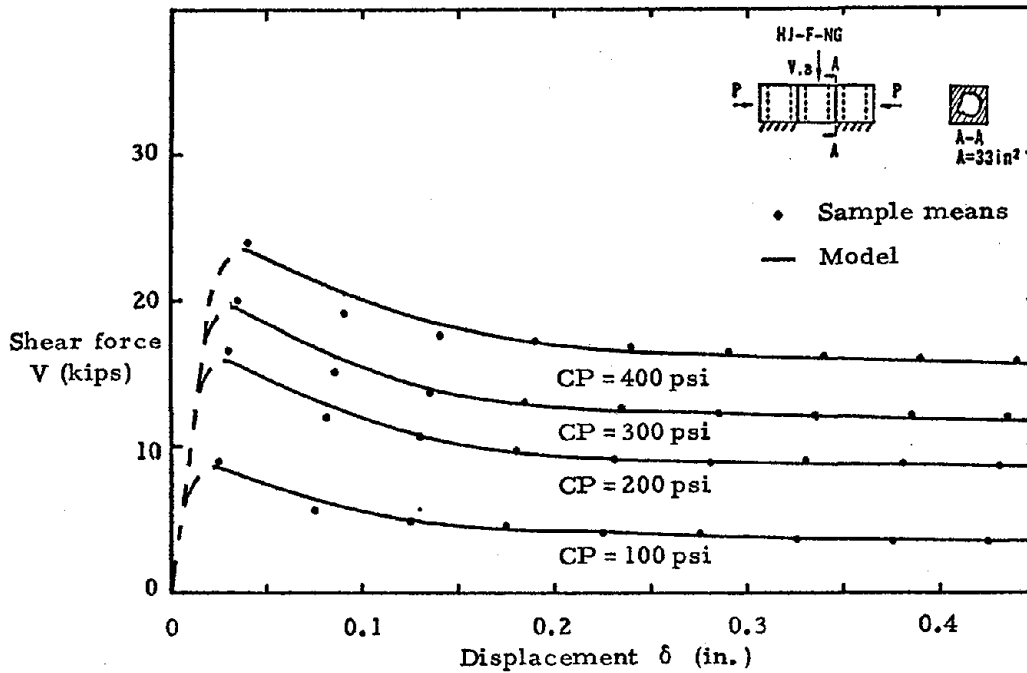


Figure 20 Comparison of model with experiment for the fully-mortared head joint.

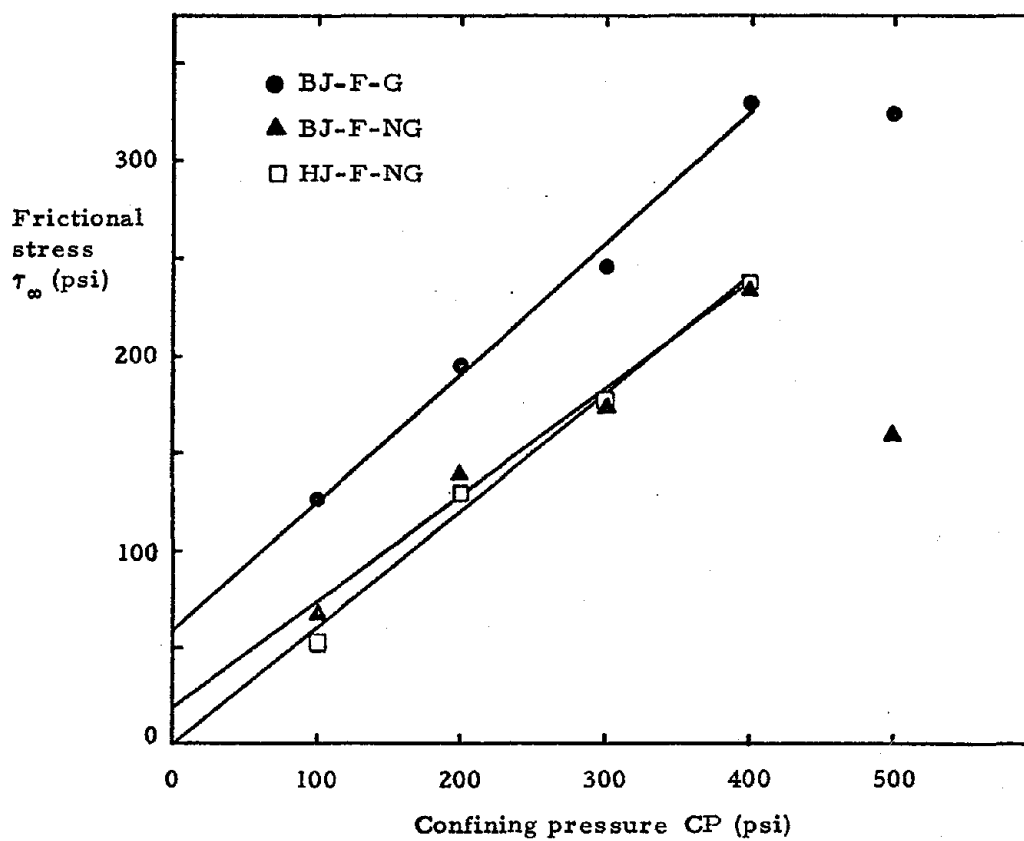
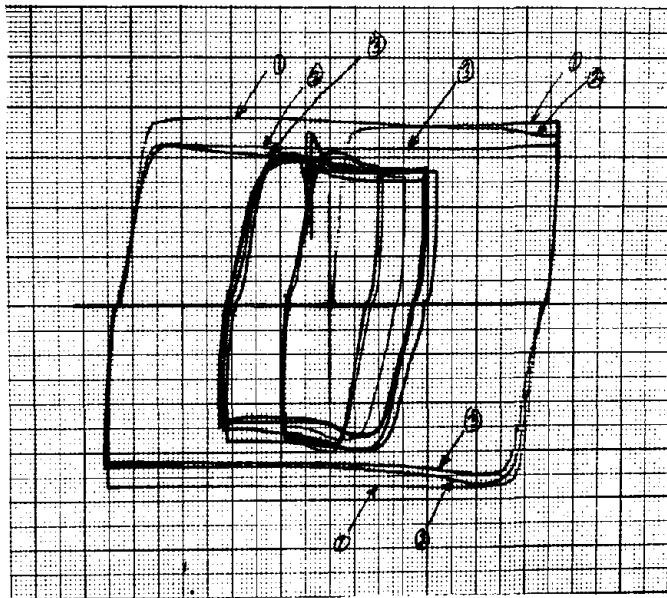


Figure 21

Predicted linear relation between frictional stress $\tau_{\infty} \equiv V_{\infty}/A$ vs. confining pressure CP for three cases of masonry joints.



Force
(2.5 Klb/cm)

Displacement (0.05 inch/cm)

Figure 22 Bidirectional shearing force versus center block displacement for 3 cycling rates where the maximum center block velocities vary over a 40 to 1 range.

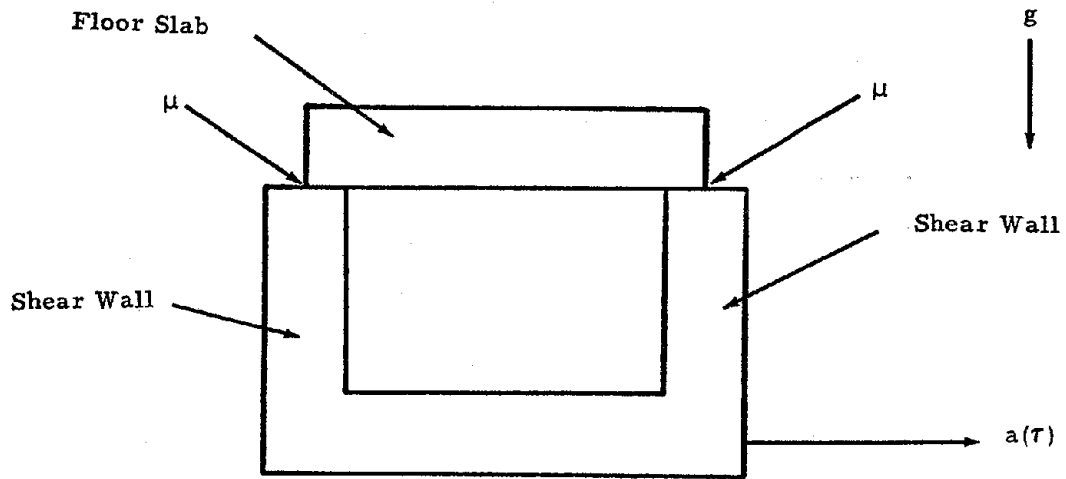


Figure 23 Configuration of the idealized wall-floor slab assemblage.

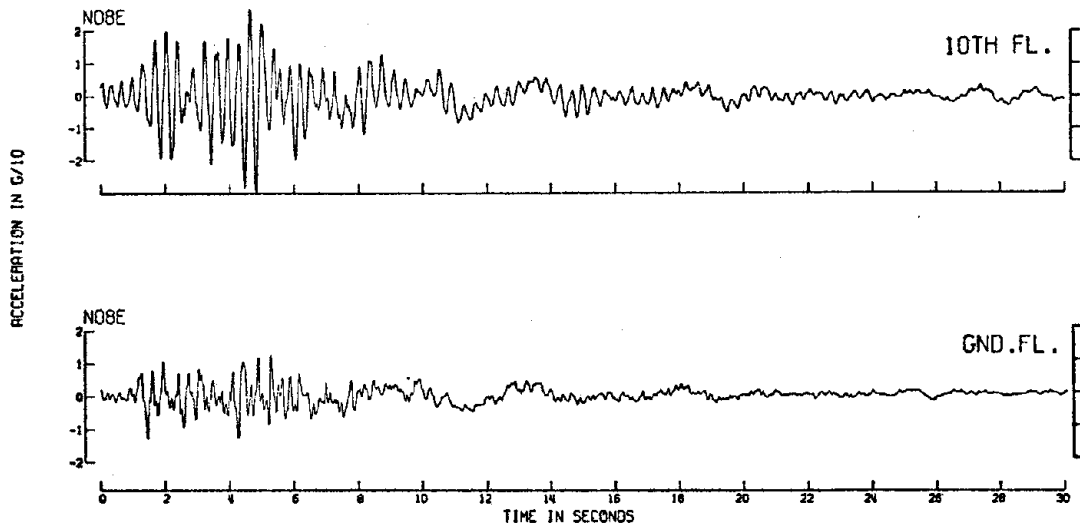


Figure 24 Comparison of the accelerograms recorded on the ground floor and on the 10th floor of 6200 Wilshire Blvd., February 9, 1971.

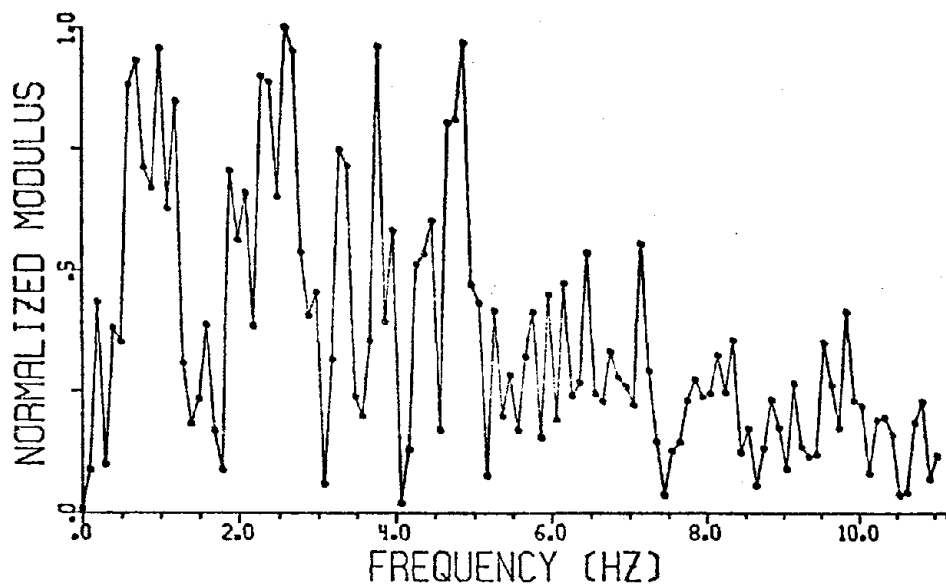


Figure 25 The spectral decomposition of the Pacoima Dam, February 9, 1971, S14W component of acceleration. The modulus of the Fourier coefficients normalized so that the largest component is 1 vs. frequency.

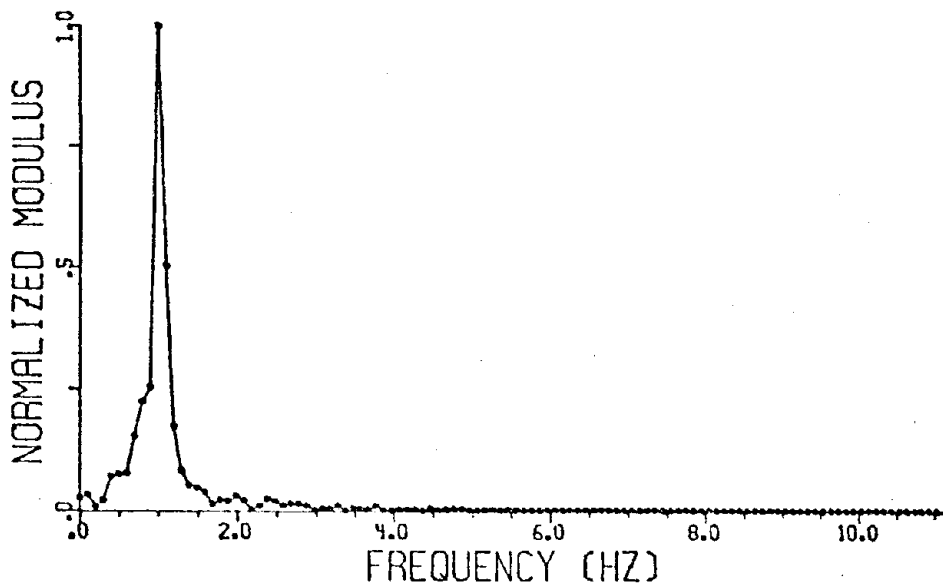


Figure 26 The spectral decomposition of the absolute acceleration of a linear oscillator, damping = 2% critical, undamped natural frequency = 1 Hz., excited by the Pacoima Dam, February 9, 1971, S14W acceleration component input. The modulus of the Fourier coefficients normalized so that the largest component is 1 vs. frequency.

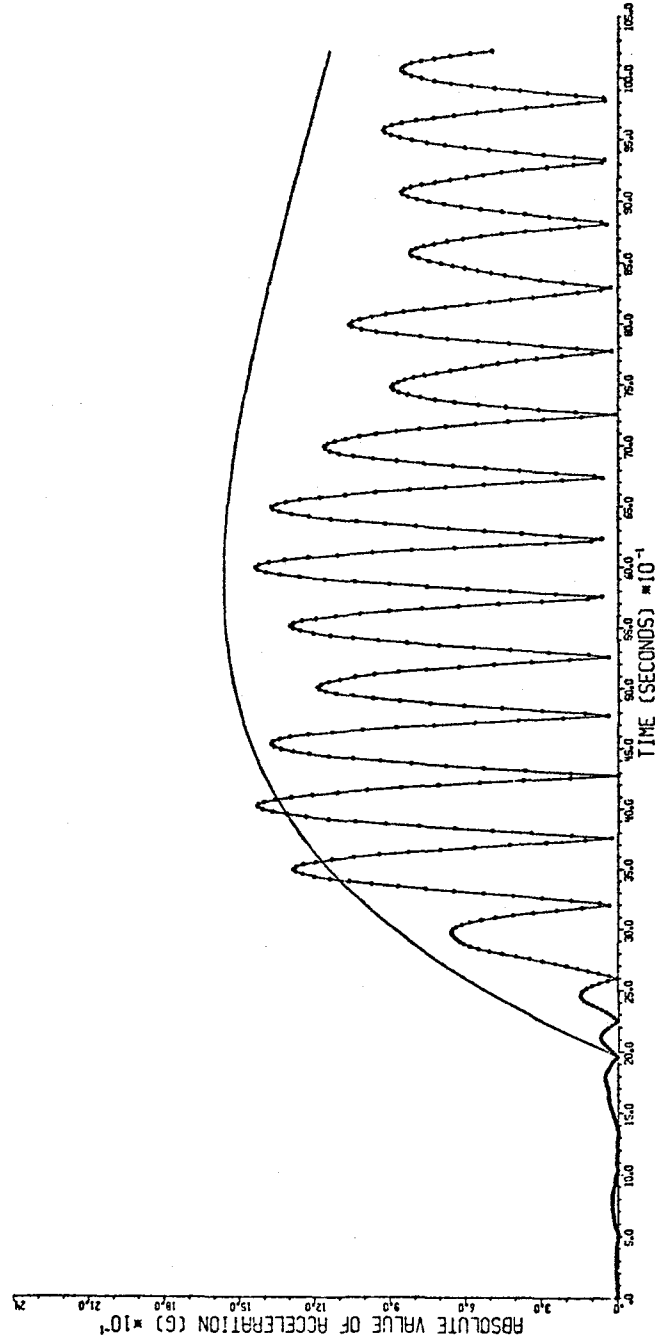


Figure 27 The absolute value of absolute acceleration of a linear oscillator, damping = 2% critical, undamped natural frequency = 1 Hz. due to the Pacoima Dam February 9, 1971 S14W component of acceleration with the moderately rising envelope superimposed vs. time.

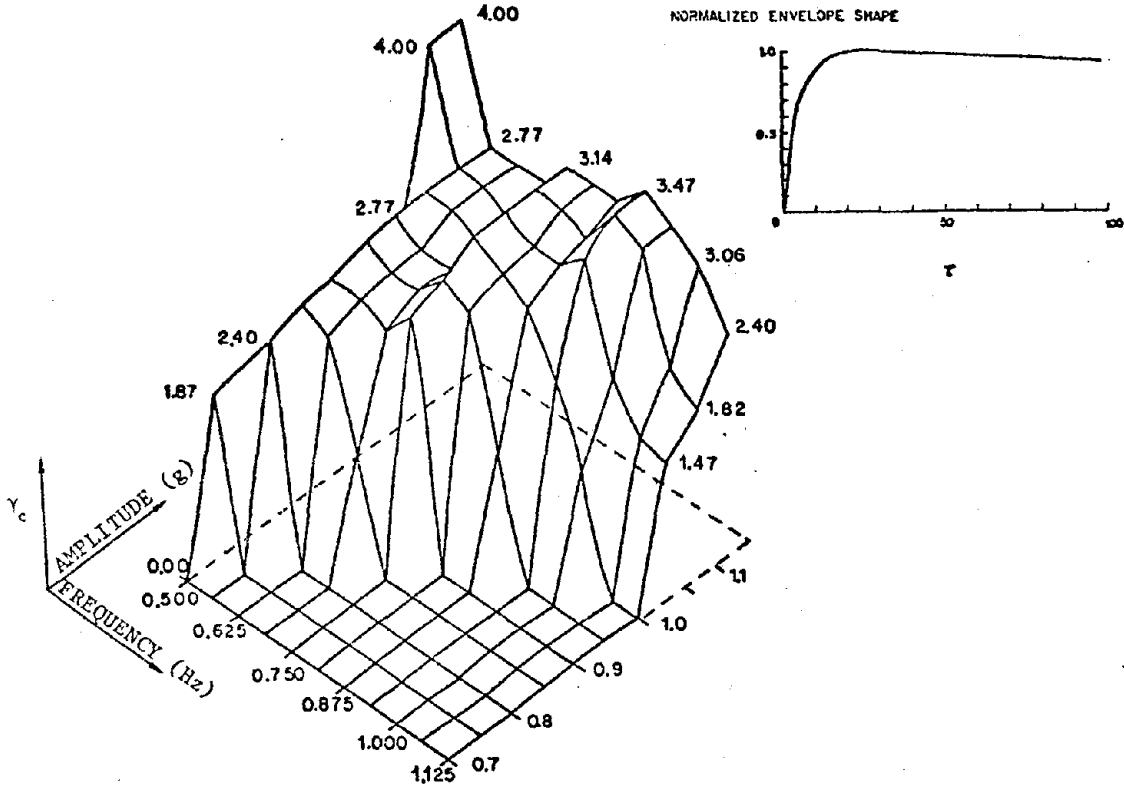


Figure 28 Surface $\gamma_c(A, f)$ for the scaling parameter τ_{max} , $\gamma_c \equiv \tau_{max}/\tau_c$, computed with the base acceleration contained in a fast rising envelope.

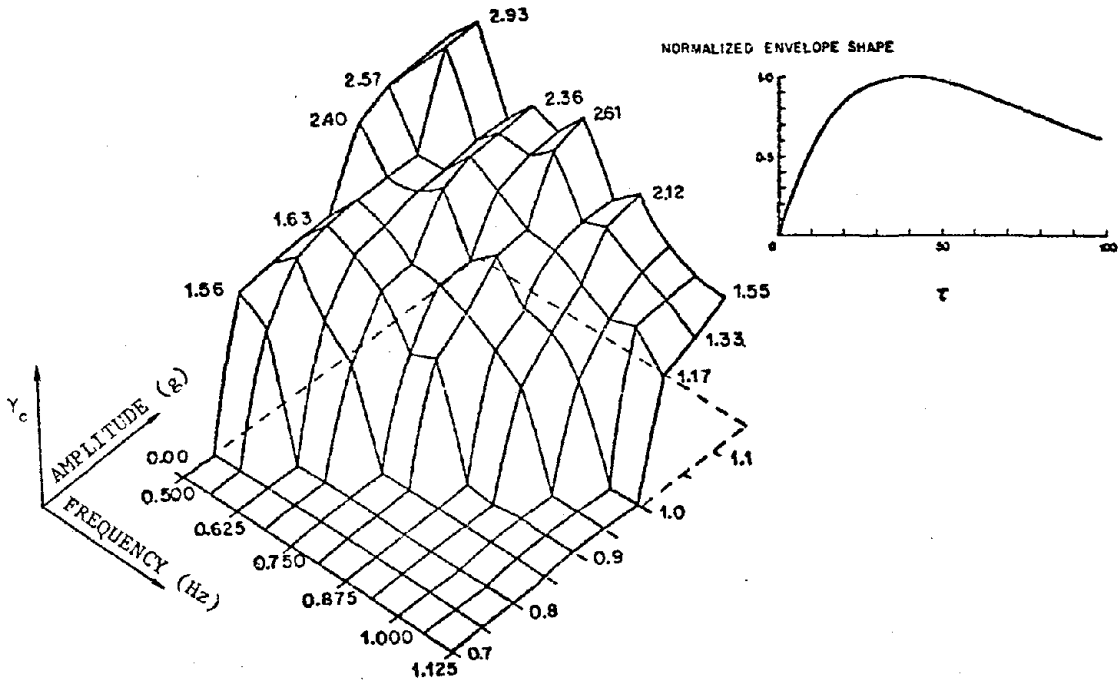


Figure 29 Surface $\gamma_c(A, f)$ for the scaling parameter τ_{max} , $\gamma_c \equiv \tau_{max}/\tau_c$, computed with the base acceleration contained in a moderately rising envelope.

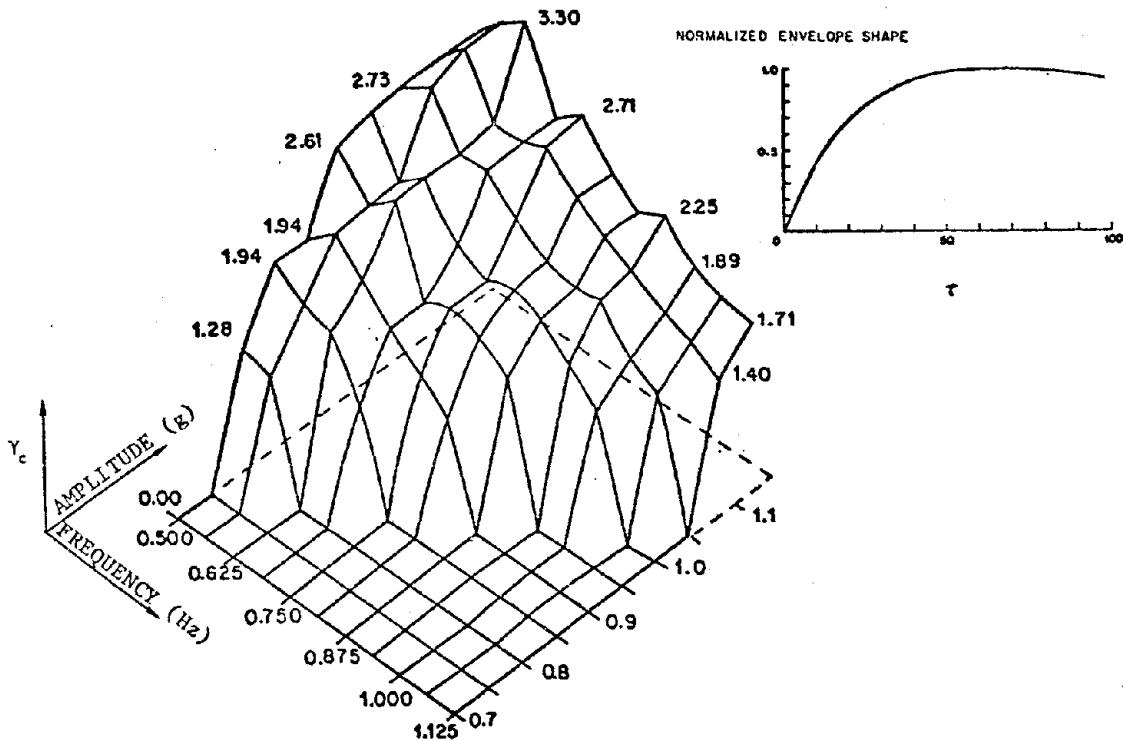


Figure 30 Surface $\gamma_c(A, f)$ for the scaling parameter τ_{max} , $\gamma_c \equiv \tau_{max}/\tau_c$, computed with the base acceleration contained in a slowly rising envelope.

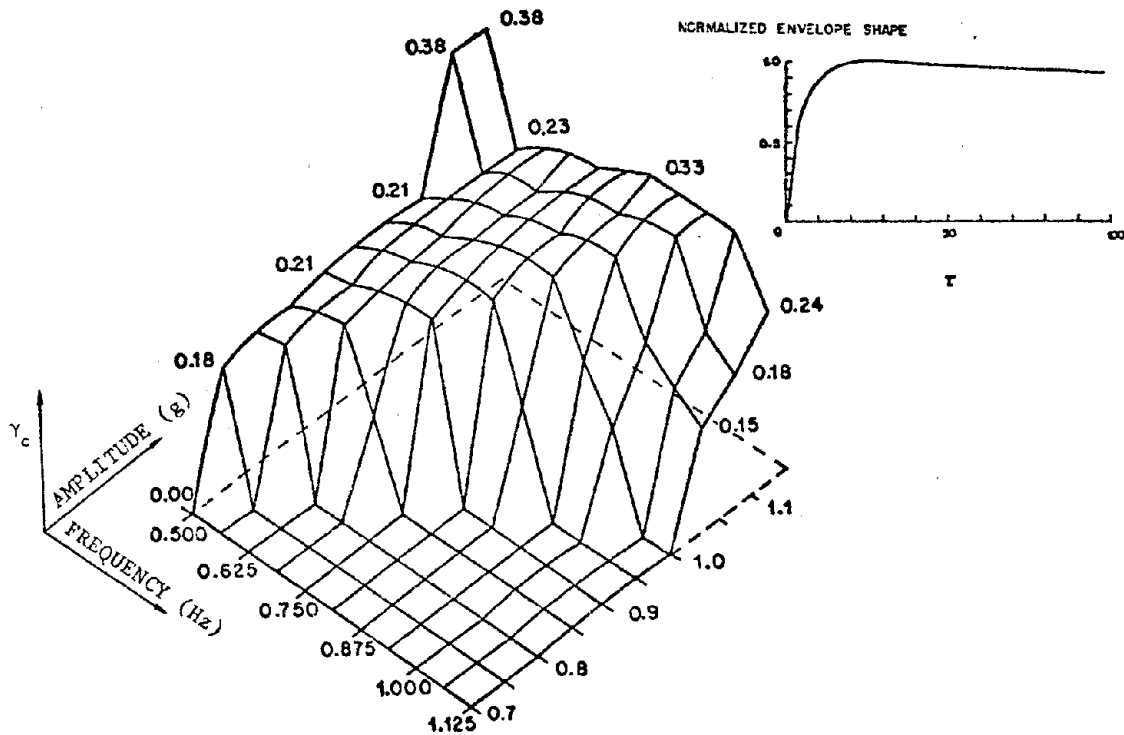


Figure 31 Surface $\gamma_c(A, f)$ for the scaling parameter τ_{rise} , $\gamma_c \equiv \tau_{rise}/\tau_c$, computed with the base acceleration contained in a fast rising envelope.

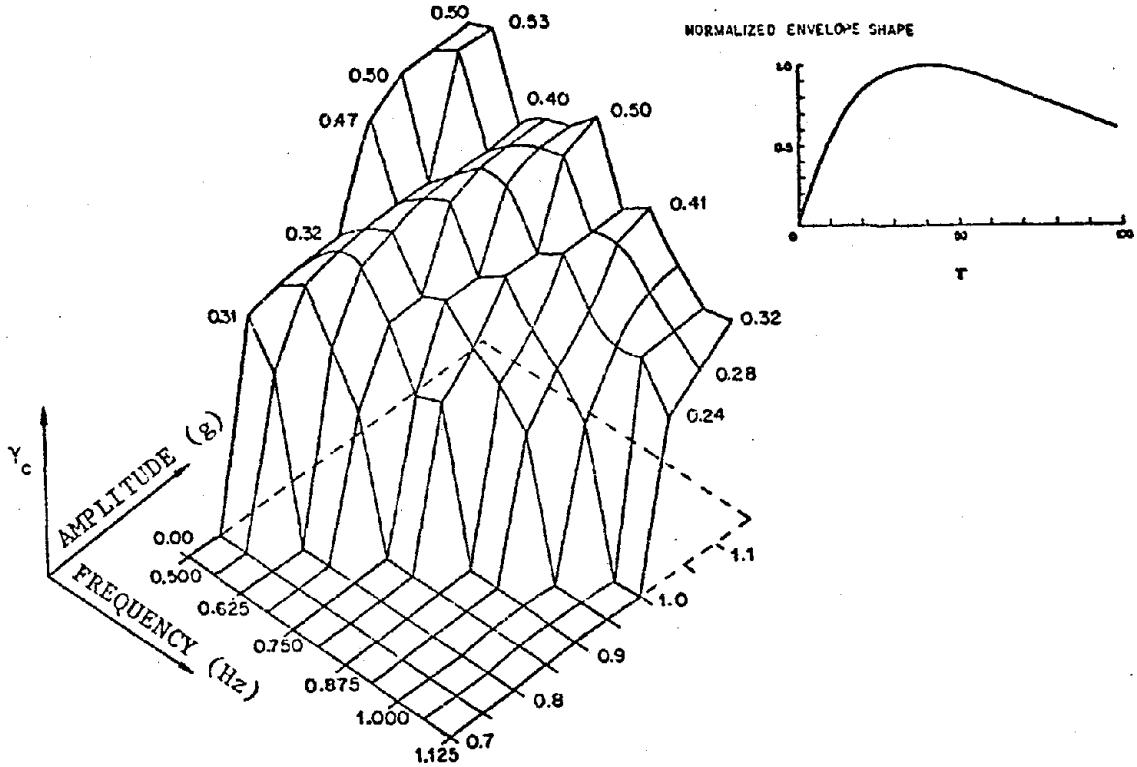


Figure 32 Surface $\gamma_c(A,f)$ for the scaling parameter τ_{rise} , $\gamma_c \equiv \tau_{rise}/\tau_c$, computed with the base acceleration contained in a moderately rising envelope.

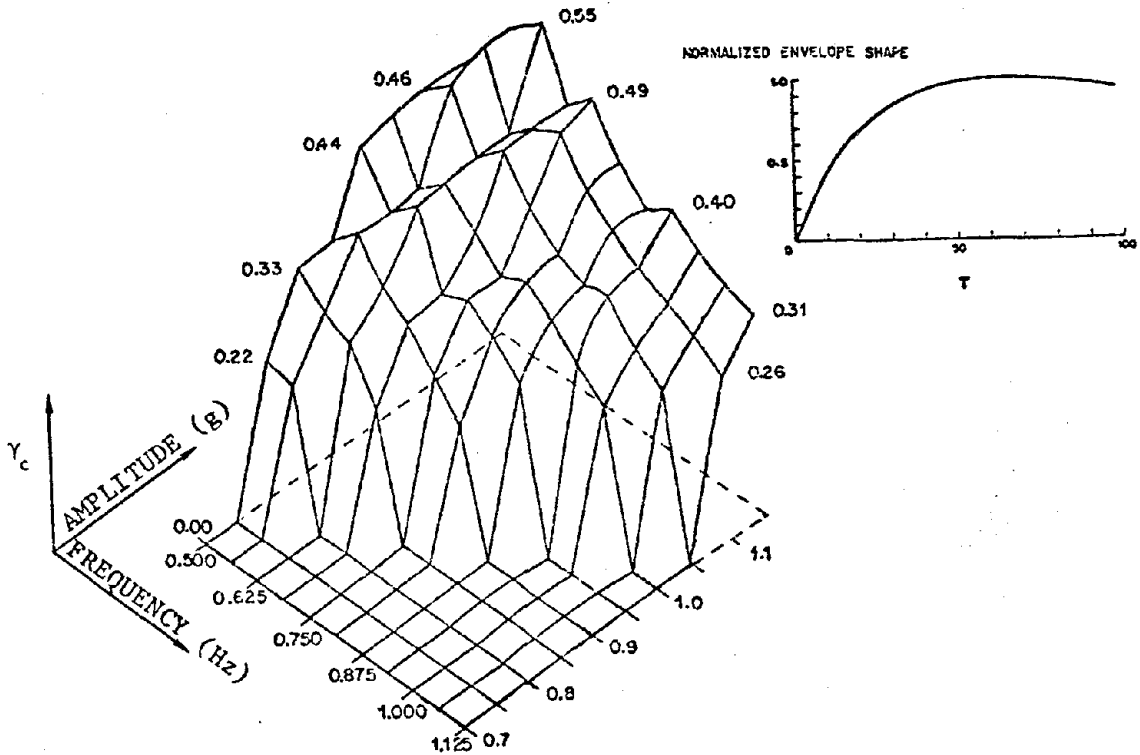


Figure 33 Surface $\gamma_c(A,f)$ for the scaling parameter τ_{rise} , $\gamma_c \equiv \tau_{rise}/\tau_c$, computed with the base acceleration contained in a slowly rising envelope.

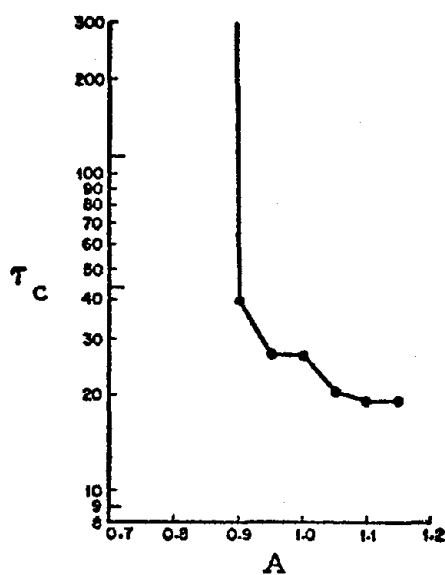


Figure 34 Nondimensional collapse time τ vs. amplitude A given fixed frequency $f = 0.75$ Hz. and moderately rising acceleration envelope.

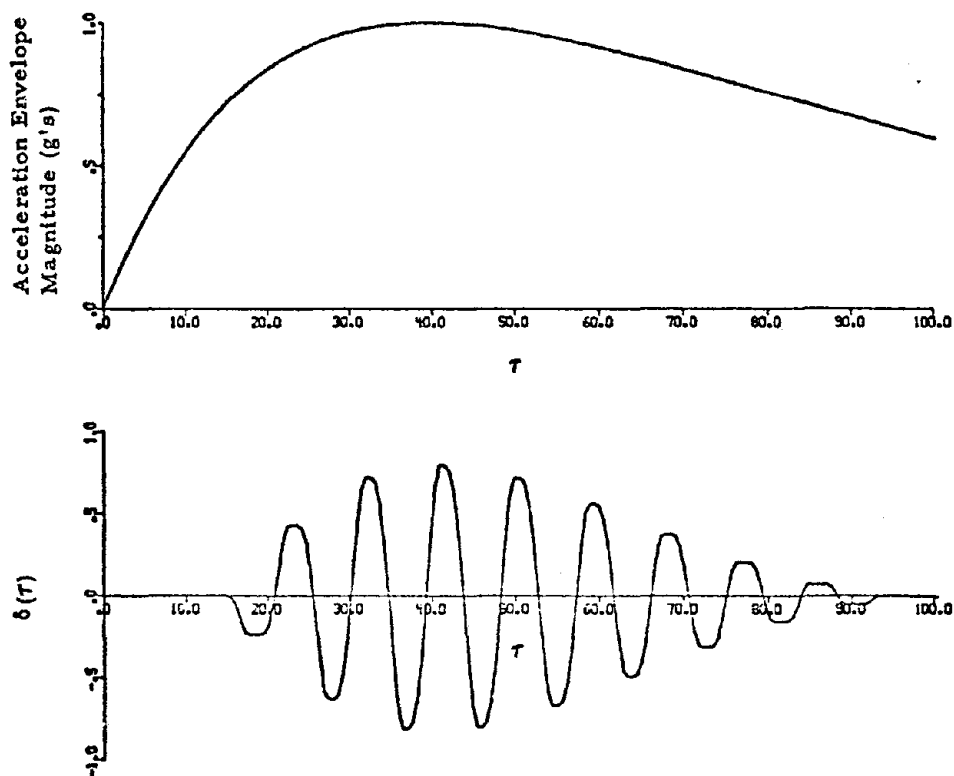


Figure 35 Nondimensional relative displacement $\delta(\tau)$ vs. nondimensional time τ with acceleration envelope vs. nondimensional time τ for $A = 1.0$, $f = 1.125$ Hz. and moderately rising acceleration envelope.

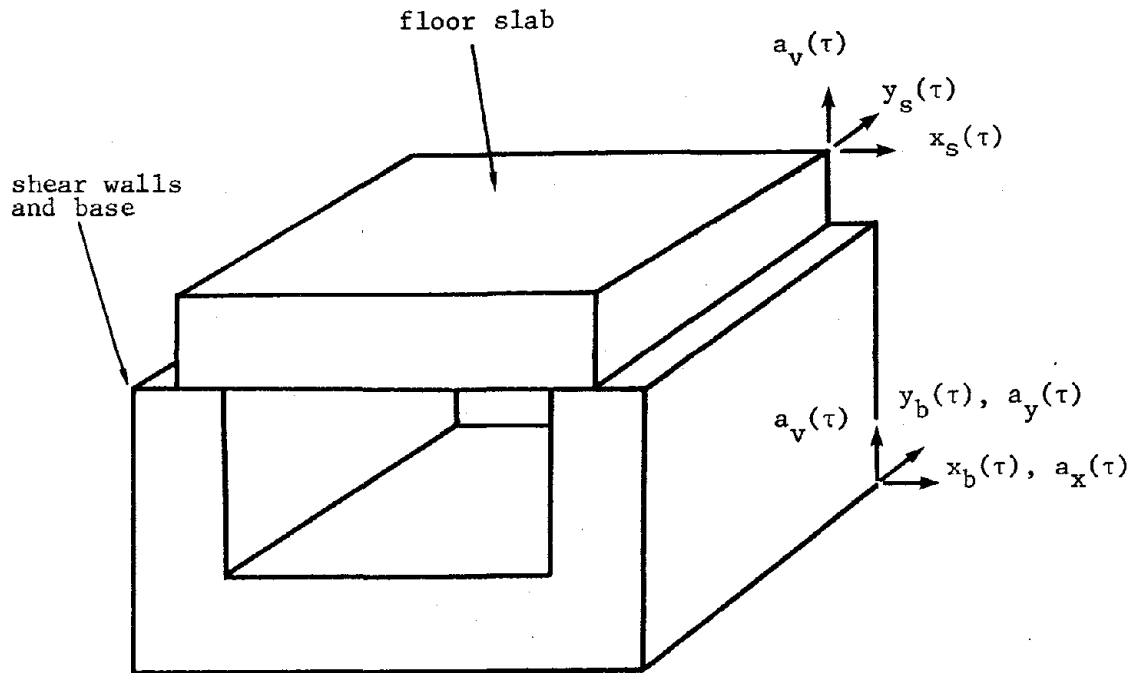


Figure 36a Floor slab-shear wall configuration for the planar motion model.

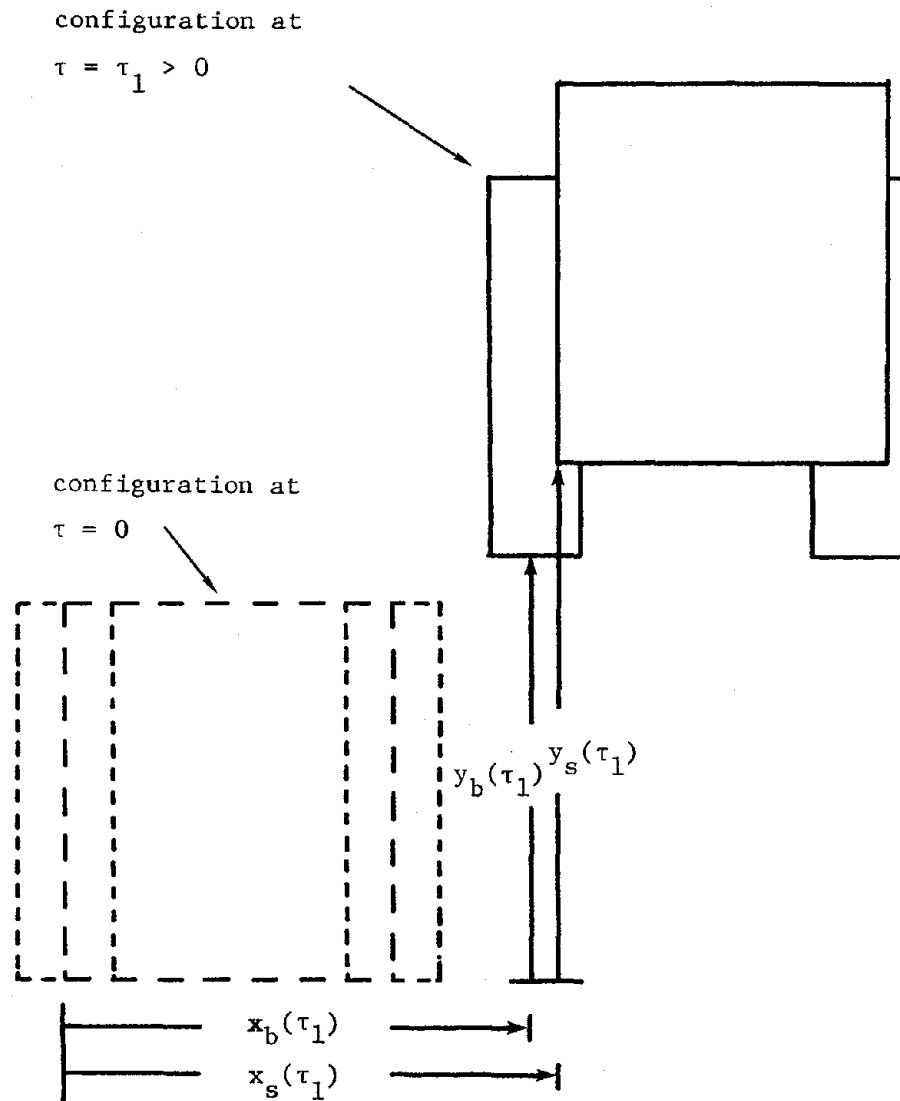


Figure 36b Top views of floor slab-shear wall configuration for the two-degree-of-freedom model at $\tau = 0$ (dotted lines) and at some later time τ_1 , $\tau_1 > 0$ (solid lines).

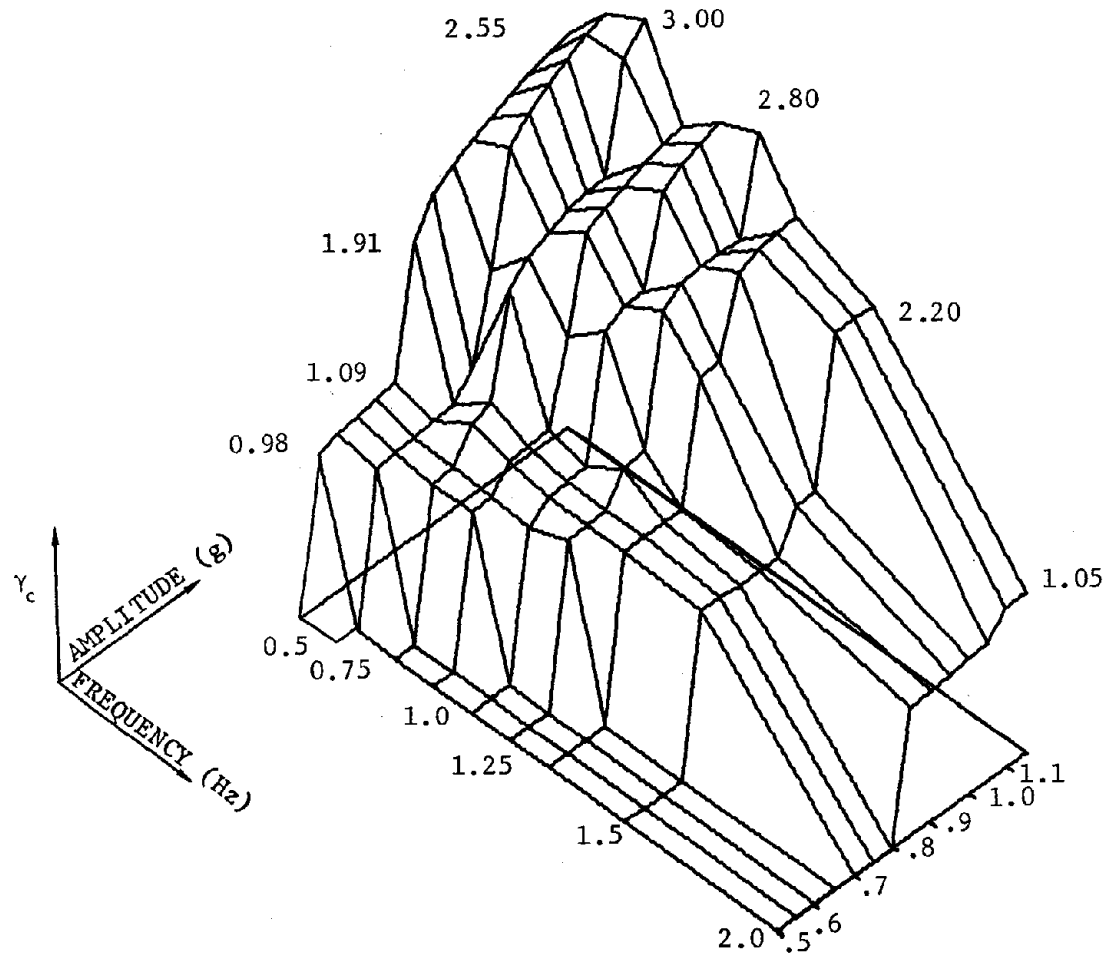


Figure 37

Surface $\gamma_c(A_x, f_x)$, $\gamma_c \equiv \tau_{\max}/\tau_c$. The result from the planar motion model with the moderately rising acceleration envelope, $A_y := 0.9 A_x$ and $f_y := 0.2$ Hz.

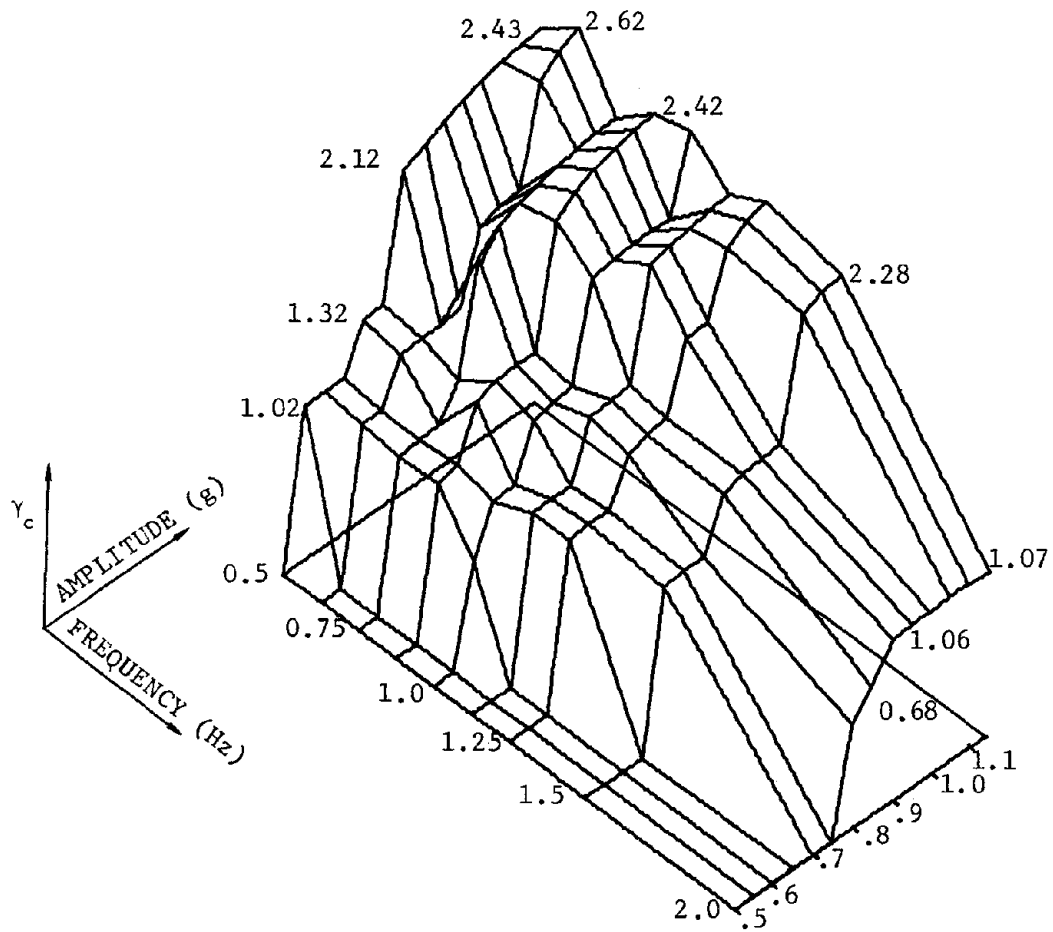


Figure 38

Surface $\gamma_c(A_x, f_x)$, $\gamma_c \equiv \tau_{\max}/\tau_c$. The result from the planar motion model with the moderately rising acceleration envelope, $A_y := 0.9 A_x$ and $f_y := 0.5$ Hz.

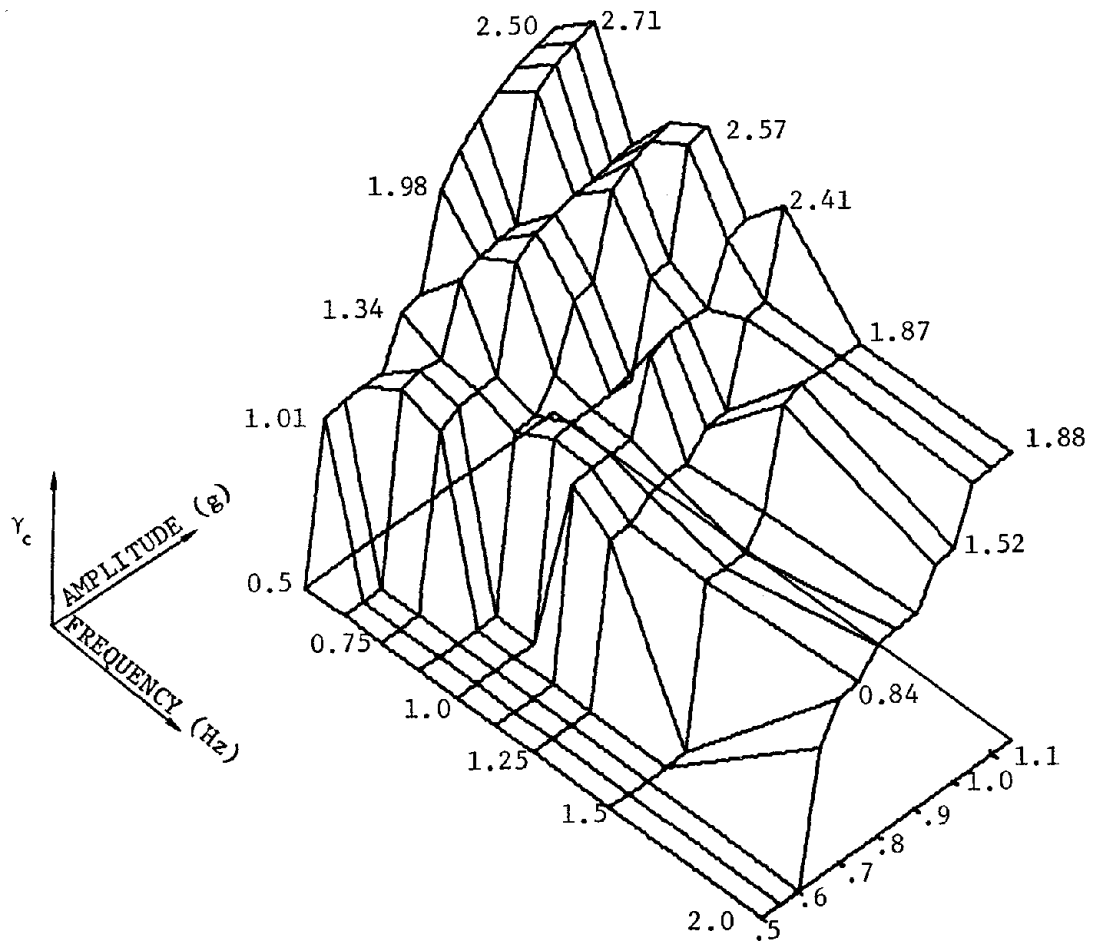


Figure 39

Surface $\gamma_c(A_x, f_x)$, $\gamma_c \equiv \tau_{\max}/\tau_c$. The result from the planar motion model with the moderately rising acceleration envelope, $A_y := 0.9 A_x$ and $f_y := 1.0$ Hz.

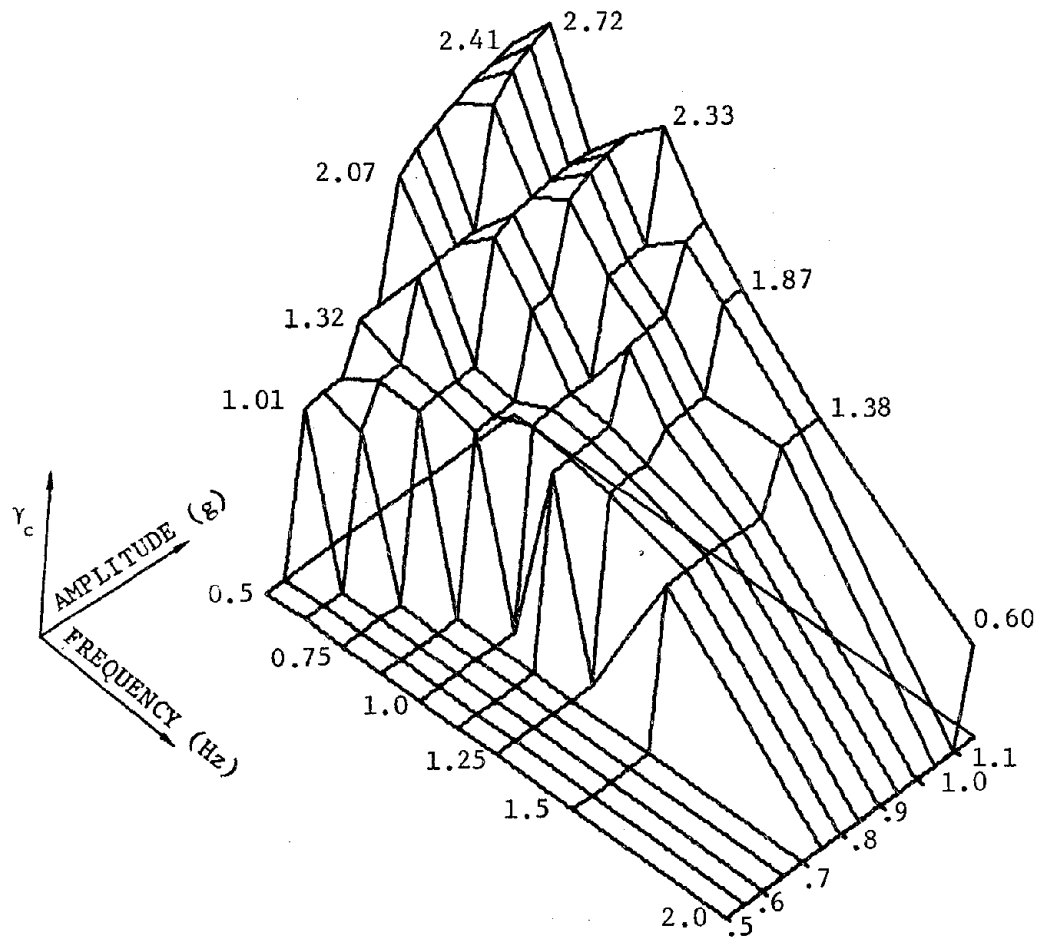


Figure 40

Surface $\gamma_c(A_x, f_x)$, $\gamma_c \equiv \tau_{\max}/\tau_c$. The result from the planar motion model with the moderately rising acceleration envelope, $A_y := 0.9 A_x$ and $f_y := 2.0$ Hz.

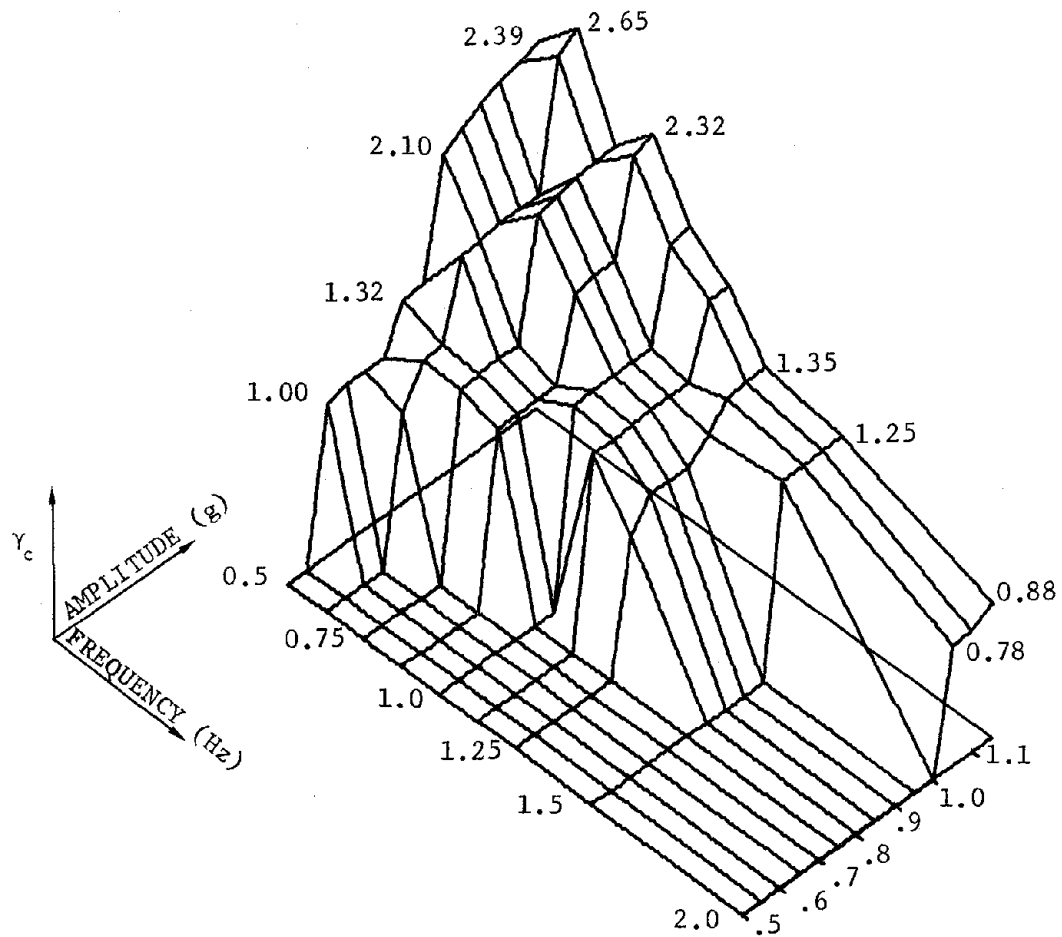


Figure 41

Surface $\gamma_c(A_x, f_x)$, $\gamma_c \equiv \tau_{\max}/\tau_c$. The result from the planar motion model with the moderately rising acceleration envelope, $A_y := 0.9 A_x$ and $f_y := 5.0$ Hz.

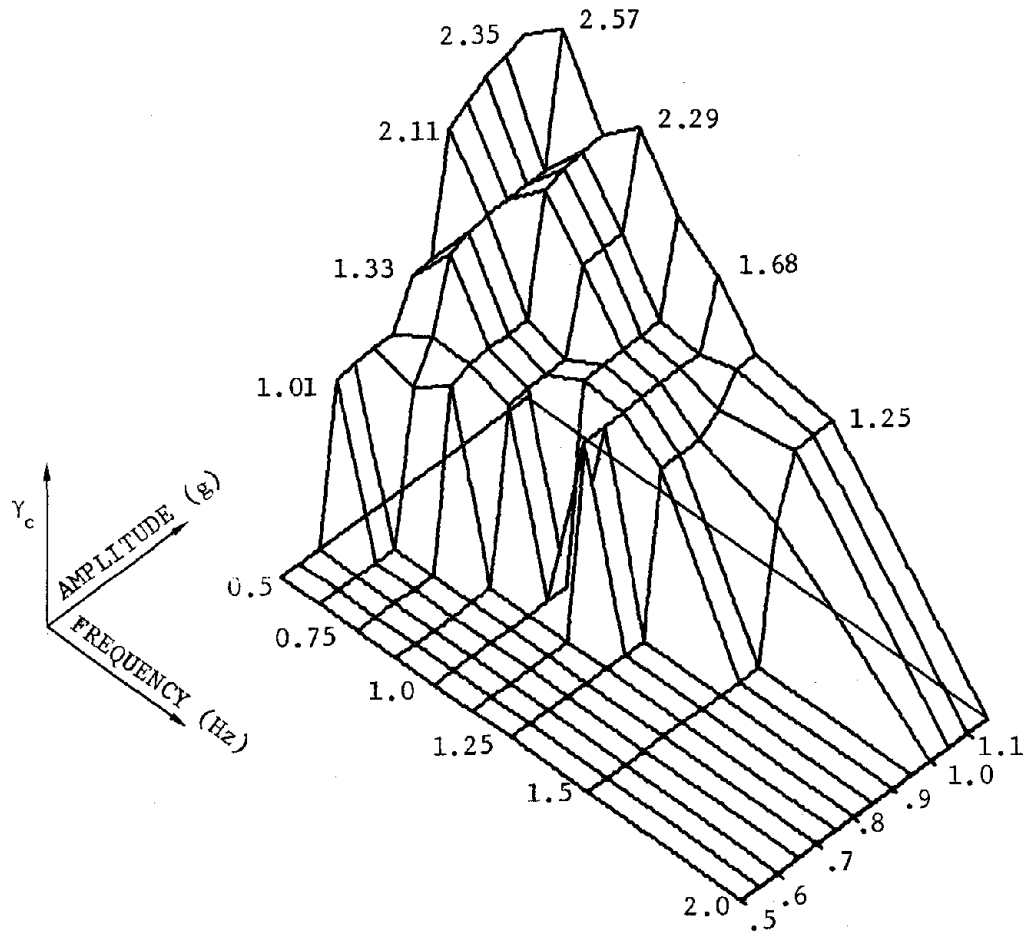


Figure 42

Surface $\gamma_c(A_x, f_x)$, $\gamma_c \equiv \tau_{\max}/\tau_c$. The result from the planar motion model with the moderately rising acceleration envelope, $A_y := 0.9 A_x$ and $f_y := 10.0$ Hz.

Table 1 Raw test data used for correlation: total shear force V_i (kips) vs. ram displacement δ_i (inches) (measured from ram displacement at peak load) test runs in three cases, BJ-F-G, BJ-F-NG, and HJ-F-NG, and for confining pressure CP = 100, 200, 300, 400, 500 (psia) in each case.

		BED JOINT GROUDED (BJ-F-G)										
		Displacement δ_i										
CP	Test No.	0	0.05	0.10	0.15	0.20	0.25	0.30	0.35	0.40		
100	{ 42	30.8	23.1	19.4	16.5	16.7	16.5	16.6	16.8	16.2		
	{ 57	-38.1	30.6	23.1	20.4	18.0	15.9	15.0	14.7	14.4		
200	{ 29	45.0	34.0	30.1	28.3	27.4	26.1	24.4	23.3	23.1		
	{ 56	44.6	33.9	31.0	27.1	26.3	25.6	24.7	23.7	23.1		
	{ 22	50.3	37.4	31.3	25.5	24.7	24.3	23.4	23.0	23.0		
300	{ 39	57.3	51.3	42.7	38.5	36.0	33.7	31.9	30.7	20.7		
	{ 44	50.0	48.0	44.7	43.5	42.5	40.6	38.8	37.0	35.5		
	{ 47	56.0	52.0	48.0	44.0	39.2	37.3	36.5	35.6	34.4		
400	{ 55	62.5	53.0	48.3	43.7	40.2	38.4	36.8	35.7	34.6		
	{ 48	65.6	62.2	54.5	48.9	46.1	43.5	41.7	40.2	39.6		
	{ 32	66.8	63.9	61.4	55.2	51.8	48.9	46.6	44.4	42.6		
500	{ 49	72.3	69.8	64.7	59.8	55.3	52.0	48.9	46.8	45.0		
	{ 34	70.3	67.8	62.5	57.0	54.0	50.9	45.0	45.5	43.6		
	{ 50	71.0	68.9	65.3	60.0	54.8	51.3	48.8	47.6	46.3		

(Table 1, continued)

Table 1, continued

BED JOINT NOT GROUTED (BJ-F-NG)

CP	Test No.	Displacement δ_i										
		0	0.05	0.10	0.15	0.20	0.25	0.30	0.35	0.40		
100	{ 19 10	6.7	5.5	5.3	4.8	4.6	4.4	4.3	4.2	4.1		
		11.3	7.9	6.8	6.1	5.5	5.1	4.9	4.8	4.8		
200	{ 30 7 43 34 36 21 11	12.2	10.3	9.7	9.3	9.1	9.0	8.8	8.6	8.3		
		20.3	16.8	14.6	14.0	13.4	13.0	12.8	12.4	12.1		
		13.1	11.1	10.6	10.3	9.9	9.9	9.9	9.9	9.8		
		17.1	12.2	10.8	10.1	9.8	9.5	9.4	9.3	9.2		
		15.5	12.4	11.4	10.8	10.2	9.7	9.3	9.0	8.7		
		15.2	12.0	10.9	10.4	9.9	9.7	9.4	9.3	9.2		
300	{ 11 38 28 27 6 44 13	16.7	12.6	11.0	10.2	9.3	8.8	8.5	8.3	8.1		
		17.0	15.3	14.4	13.6	12.6	11.2	10.7	10.4	10.0		
		17.4	15.7	14.6	13.5	12.4	11.4	10.3	9.3	8.8		
		18.7	14.2	13.2	12.3	11.5	10.4	9.4	9.4	8.9		
		19.3	14.7	13.7	13.7	13.2	12.9	12.5	12.3	12.2		
		21.1	15.5	13.6	12.8	12.5	12.3	12.0	11.8	11.5		
400	{ 48 2 3	18.5	15.3	13.5	12.7	12.2	11.7	11.3	11.1	10.9		
		22.4	18.3	17.1	15.7	14.2	12.5	11.1	10.1	9.0		
		30.6	22.5	21.2	20.4	19.8	19.3	18.8	18.2	17.9		
500	{ 5 4 3	27.3	22.0	20.4	19.8	19.3	18.8	18.5	18.3	18.0		
		28.1	24.3	25.4	25.0	24.3	23.2	22.2	20.7	18.8		
		28.4	24.0	23.2	22.1	21.2	20.2	18.4	16.2	15.4		
		25.1	22.3	19.5	17.4	16.0	14.4	13.5	13.1			

(Table 1, continued)

Table 1, continued

HEAD JOINT NOT GROUDED (HJ-F-NG)

CP	Test No.	Displacement δ_i										
		0	0.05	0.10	0.15	0.20	0.25	0.30	0.35	0.40		
100	{ 42 43	8.3	5.2	4.4	3.9	3.6	3.5	3.5	3.4	3.4	3.4	
		9.4	6.8	6.2	5.3	4.8	4.4	4.2	4.0	3.8		
200	{ 11 22 35	15.3	10.7	9.5	9.0	8.8	8.6	8.5	8.4	8.3		
		17.9	12.9	10.9	9.	9.1	8.	8.6	8.	8.3		
		18.5	13.3	11.1	10.3	9.8	9.3	9.1	8.9	8.7		
300	{ 13 3 31	19.5	14.4	13.0	12.6	12.2	12.2	12.2	12.1	12.1		
		21.4	15.8	14.5	13.8	13.3	12.9	12.6	12.4	12.3		
		19.7	14.9	12.9	12.2	12.1	11.8	11.8	11.7	11.6		
400	{ 14 5 15	23.0	19.5	18.0	17.3	17.0	16.7	16.4	16.0	15.9		
		22.7	18.9	17.5	16.8	16.6	16.3	16.0	15.6	15.0		
		24.2	19.4	17.5	17.2	17.1	16.9	16.7	15.9	15.0		

Table 2 Summary of best-fit values for regression parameters V_{∞} , c , and b , fitted to the sample mean values of V_i for each test, for three cases and five confining pressures.

BJ-F-G

CP	V_1	V_9	b	c	V_{∞}	Bounds on minimization errors for V_{∞}	f_m	$V_1 - V(\delta_1)$
100	34.0	15.0	-0.01	10.11	14.6	± 0.19	0.07	-0.20
200	45.5	23.5	-0.00	7.92	22.6	± 0.29	0.03	-0.09
300	54.0	33.1	-0.02	4.36	28.5	± 0.42	0.10	-0.40
400	66.0	39.2	*0.03	*3.91	*38.2	± 0.50	0.22	0.76
500	71.2	45.5	*0.01	*1.75	*37.5	± 0.57	0.22	-0.22

BJ-F-NG

100	9.0	4.5	0.03	10.84	4.4	± 0.06	0.03	0.11
200	15.0	8.9	0.03	10.79	8.9	± 0.12	0.06	0.24
300	19.6	11.5	0.04	10.26	11.5	± 0.10	0.20	0.33
400	26.5	15.7	0.03	8.35	15.5	± 0.20	0.11	0.35
500	27.0	15.8	0.03	2.69	10.7	± 0.60	0.10	0.42

HJ-F-NG

100	9.0	3.5	0.04	11.04	3.5	± 0.05	0.10	0.24
200	16.5	8.6	0.02	12.44	8.5	± 0.11	0.05	0.19
300	20.0	11.9	0.04	12.04	11.8	± 0.15	0.15	0.32
400	24.0	15.8	0.05	10.72	15.6	± 0.20	0.23	0.40

* Best fit obtained with $\beta = 1/3$.

Table 3 Statistical analysis of 7 runs of test BJ-F-NG-200.

Table 3a Calculation of regression parameters V_∞ , c , and b for each run, and comparison of the figures of merit f_m for $\alpha = 2$, $\beta = 0$, and for $\alpha = 2$, $\beta = 1/3$.

δ (inches)	#30	#7	#43	#34	#36	#21	#11
0	12.2	20.3	13.1	17.1	15.5	15.2	16.7
0.05	10.3	16.8	11.1	12.2	12.4	12.0	12.6
0.10	9.7	14.6	10.6	10.8	11.4	10.9	11.0
0.15	9.3	14.0	10.3	10.1	10.8	10.4	10.2
0.20	9.1	13.4	9.9	9.8	10.2	9.9	9.3
0.25	9.0	13.0	9.9	9.5	9.7	9.7	8.8
0.30	8.8	12.8	9.9	9.4	9.3	9.4	8.5
0.35	8.6	12.4	9.9	9.3	9.0	9.3	8.3
0.40	8.3	12.1	9.8	9.2	8.7	9.2	8.1

 $\alpha = 2, \beta = 0$

b	0.06	0.03	0.02	0.02	0.04	0.03	0.02
c	7.80	9.58	14.67	15.48	8.23	11.48	10.16
$V_\infty \begin{cases} +10^{-6} \\ -0.6 \end{cases}$	8.25	12.08	9.80	9.21	8.70	9.20	8.08
f_m	0.06	0.07	0.01	0.05	0.08	0.04	0.05

 $\alpha = 2, \beta = 1/3$

b	0.12	0.08	0.06	0.05	0.09	0.07	0.07
c	7.57	8.50	16.37	16.92	8.00	12.06	10.49
$V_\infty \begin{cases} +10^{-6} \\ -0.6 \end{cases}$	8.25	12.08	9.80	9.21	8.70	9.20	8.08
f_m	0.15	0.32	0.05	0.26	0.26	0.17	0.27

Table 3b Comparison of values obtained for regression parameters V_{∞} , c and b as determined by:

- i) means of values as calculated from each of 7 runs in Table 3a

$$\bar{V}_{\infty} = 9.33 , \quad \hat{\sigma}^2 = 1.82 , \quad \hat{\sigma} = 1.35 ,$$

- ii) means of values as calculated from each of 6 runs (omitting run #7) in Table 3a

$$\bar{V}_{\infty} = 8.87 , \quad \hat{\sigma}^2 = 0.43 , \quad \hat{\sigma} = 0.65 ,$$

- iii) sample mean values for 7 runs: see below.

- iv) sample mean values for 6 runs (omitting run #7—same values as in Table No. 2): see below.

	(iii)	(iv)
δ_i	V_i	V_i
0	15.3	15.0
0.05	12.3	11.8
0.10	11.1	10.2
0.15	10.4	10.2
0.20	10.2	9.7
0.25	9.8	9.4
0.30	9.7	9.2
0.35	9.4	9.0
0.40	9.3	8.9
$V_{\infty} \rightarrow$	9.13 ± 0.12	$8.87 \begin{cases} +10^{-6} \\ -0.09 \end{cases}$
c \rightarrow	9.73	10.79
b \rightarrow	0.039	.033

Table 3c Confidence intervals for mean \bar{V}_∞ , variance $\hat{\sigma}^2$, and standard deviation $\hat{\sigma}$ for V_∞ as calculated for each run in a sample size of 6 runs (omitting run #7).

Confidence interval	$\hat{\sigma}^2$ and $(\hat{\sigma})$	\bar{V}_∞	" χ^2 " distr. for 5 DOF	"t" distr. for 5 DOF
1-99	0.141 < 0.425 < 3.839 (0.375 < 0.652 < 1.959)	7.977 < 8.8733 < 9.769	15.1 (.554)	3.365
5-95	0.192 < 0.425 < 1.849 (0.438 < 0.652 < 1.360)	8.337 < 8.8733 < 9.410	11.1 (1.15)	2.015
10-90	0.230 < 0.425 < 1.321 (0.480 < 0.652 < 1.149)	8.480 < 8.8733 < 9.266	9.24 (1.61)	1.476

With sample size n ,

Confidence interval for variance $\left[\frac{(n-1)\hat{\sigma}^2}{a}, \frac{(n-1)\hat{\sigma}^2}{b} \right]$, a & b percentile point of " χ^2 " distribution

Confidence interval for mean $\left[\bar{V}_\infty - \frac{\tau\hat{\sigma}}{\sqrt{n}}, \bar{V}_\infty + \frac{\tau\hat{\sigma}}{\sqrt{n}} \right]$, τ percentile point of "t" distribution

Note that $\bar{V}_{\infty \text{ mean}} = 9.13$ predicted from sample mean lies inside 98% confidence interval.

Table 4 The correspondence between the chosen nondimensional characteristic times and real time for an "8 inch" wall, $t^* = 0.099$.

	Nondimensional Time	Real Time (seconds)
<u>fast rising envelope</u>		
	$\tau_{\text{rise}} = 3.38$	0.33
	$\tau_{\text{max}} = 27.78$	2.75
	$\tau_{\text{dur}} = 732.11$	72.48
<u>moderately rising envelope</u>		
	$\tau_{\text{rise}} = 8.92$	0.88
	$\tau_{\text{max}} = 37.89$	3.75
	$\tau_{\text{dur}} = 113.80$	11.27
<u>slow rising envelope</u>		
	$\tau_{\text{rise}} = 12.81$	1.27
	$\tau_{\text{max}} = 63.13$	6.25
	$\tau_{\text{dur}} = 266.23$	26.36

APPENDIX

The following is a more detailed description and flow chart of the constituent parts of a computer program which integrates equations of motion involving Coulomb friction between rigid bodies.

CALCULATION OF THE BASE ACCELERATION, $a(\tau)$

To prescribe the acceleration,

$$a(\tau) = \frac{2 g A (t^*)^2}{d S_{\max}} (\exp (- \alpha t^* \tau) - \exp (- \beta t^* \tau)) \sin \omega \tau$$

S_{\max} must be computed.

$$S_{\max} \equiv \max_{\tau > 0} | (\exp (- \alpha t^* \tau) - \exp (- \beta t^* \tau)) \sin \omega \tau |$$

A subroutine computes the successive peaks of the oscillations of

$$| (\exp (- \alpha t^* \tau) - \exp (- \beta t^* \tau)) \sin \omega \tau |$$

This is done by applying a Newton iteration to find τ_{peak} , the time of successive local extrema, such that

$$\frac{d}{d\tau} \left[(\exp (- \alpha t^* \tau) - \exp (- \beta t^* \tau)) \sin \omega \tau_{\text{peak}} \right] = 0$$

then evaluating

$$| (\exp (- \alpha t^* \tau) - \exp (- \beta t^* \tau)) \sin \omega \tau |$$

at τ_{peak} . Because $(\exp (- \alpha t^* \tau) - \exp (- \beta t^* \tau))$ monotonically increases to a maximum and monotonically decreases thereafter, the successive peaks of

$$| (\exp (- \alpha t^* \tau) - \exp (- \beta t^* \tau)) \sin \omega \tau |$$

will also increase monotonically to a maximum then monotonically decrease. The code computes successive peaks until a local peak decreases, then the previous peak is taken as S_{\max} . Taking

$$\left[\left(1 / (4 f t^*) \right) + \left((N - 1) / (2 f t^*) \right) \right]$$

as the initial guess for the N^{th} local extremum was satisfactory. Examining successive Newton iterates shows that convergence is very fast; 3 iterations generally reduces the relative error to less than 10^{-5} .

MAIN PROGRAM

With $a(\tau)$ prescribed, the code sets the integration step size, H , to $1 / 16$ the oscillatory period and tests the initial conditions on the displacements and velocities of the floor slab and walls to determine if the floor slab is sliding or not. A flag is conditioned accordingly. An integration step is taken with step size equal $H / 2$ to develop a data base for polynomial approximation of wall and slab velocities. The motion regime, slipping or sticking, may not change during this integration step. For $\tau > H / 2$, no restrictions on where the motion regime may change are imposed other than that the regime may change only once per step of size H . Marching proceeds with tests for change of regime at each step until $|y_b - y_s| > 1$, indicating collapse or until $\tau > \tau_{\text{out}}$, a time before which any assembly collapse must take place.

METHOD OF INTEGRATION

The integration scheme is a 4^{th} order Runge-Kutta method, an implementation of the following algorithm¹:

$$\underline{y}(\tau) \equiv \begin{bmatrix} y_b(\tau) \\ \dot{y}_b(\tau) \\ y_s(\tau) \\ \dot{y}_s(\tau) \end{bmatrix}$$

to solve $\dot{\underline{y}}(\tau) = \underline{f}(\tau, \underline{y})$ with step size H , knowing

$$\begin{aligned} \underline{y}_n &= \underline{y}(\tau_n), \quad \tau_n = nH \\ \underline{K}_1 &= H \underline{f}(\tau_n, \underline{y}_n) \end{aligned}$$

$$\begin{aligned}
\underline{K}_2 &= H \underline{f} (\tau_n + H/2, \underline{y}_n + \underline{K}_1/2) \\
\underline{K}_3 &= H \underline{f} (\tau_n + H/2, \underline{y}_n + \underline{K}_2/2) \\
\underline{K}_4 &= H \underline{f} (\tau_n + H, \underline{y}_n + \underline{K}_3) \\
\underline{y}_{n+1} &= \underline{y}_n + (\underline{K}_1 + 2\underline{K}_2 + 2\underline{K}_3 + \underline{K}_4)/6
\end{aligned}$$

The integration subroutine returns with $y_s(\tau + H)$, $\dot{y}_s(\tau + H)$, $y_b(\tau + H)$, $\dot{y}_b(\tau + H)$, and $\tau \leftarrow \tau + H$.

TEST FOR SLIPPING

When the magnitude of the base acceleration $|a(\tau)|$ exceeds a_s , the floor slab will slip on the walls. It is necessary to check the magnitude of $a(\tau)$ at each integration step. Assume that the floor slab is not slipping on the walls. Should $|a(\tau)|$ exceed a_s in the interval, the time of slipping, τ_{slip} such that

$$|a(\tau_{\text{slip}})| = a_s,$$

must be located. A Newton iteration is used to locate τ_{slip} such that

$$\tau - H < \tau_{\text{slip}} < \tau \quad \text{and} \quad |a(\tau_{\text{slip}})| - a_s = 0$$

using $\tau - H/2$ as the initial guess to τ_{slip} . Iteration is continued until the Newton correction is less than 10^{-6} . The convergence is typically very fast with the convergence criterion being met in about 3 iterations. Convergence to $\tau - H < \tau_{\text{slip}} < \tau$ or not meeting the convergence criterion in 10 iterations is regarded as program failure. Action taken in this event is discussed later. Once τ_{slip} is located, $y(\tau - H)$ is recalled from storage, and the equations of motion for slipping are integrated from τ_{slip} to τ . $\underline{y}(\tau)$ is stored, and marching continues in the slipping regime.

TEST FOR STICKING

Assume that the floor slab is slipping on the walls. As $a(\tau)$ decreases to below a_s , Coulomb friction slows the sliding floor slab until the velocity of the base and the floor slab are equal, that is, when the base and floor slab stick together somewhere in the interval. Because the equations are initially integrated to the

end of the interval with an acceleration governed by Coulomb friction and the remainder of the interval with the smaller acceleration $a(\tau)$, the velocity change of the floor slab will be greater than it should be. This will cause the difference of base and floor slab velocities to change sign by the end of the interval. If $a(\tau) < a_s$ and the difference in base and floor slab velocities changes sign in an interval, sticking takes place in the interval. To locate

$$\tau - H < \tau_{stick} < \tau,$$

the base and floor slab velocities are approximated by quadratic polynomials generated by divided differences². The difference of base and slab velocities is manipulated into the form

$$a\tau^2 + b\tau + c = 0.$$

The quadratic formula is used to calculate one of the roots, depending on the sign of b to minimize cancellation errors. The fact that the product of the roots equals c gives the second root. If the first root lies in $[\tau - H, \tau]$, it is taken as τ_{stick} . Otherwise, the second root is taken as τ_{stick} if it lies in $[\tau - H, \tau]$. If neither root lies in the interval, the program is considered to have failed. Finding a root in the interval is the most sensitive of program functions. Many more program repetitions with reduced step size were necessitated by failure here than in failure to find a time of slipping, τ_{slip} . Nevertheless, once a root, τ_{stick} , in the interval is found, $\underline{y}(\tau - H)$ is recalled from storage, and the equations of motion for sliding are integrated from $\tau - H$ to τ_{stick} . $\underline{y}(\tau_{stick})$ is stored, and the equations of motion for sticking are integrated from τ_{stick} to τ . $\underline{y}(\tau)$ is stored and marching continues as usual in the sticking regime.

PROGRAM FAILURE

In the event that τ_{slip} or τ_{stick} cannot be found, $H / 4$ is taken as the step size and the entire calculation is repeated from the beginning. If failure occurs 3 times, then the code abandons this case of A and f.

FLOW CHART

Flow charts of the driver program and subroutine functions of the computer code follow.

REFERENCES

Dahlquist, G., A. Björck, Numerical Methods, Prentice-Hall, Englewood Cliffs, N.J., 1974.

Shampine, L.F., M.K. Gordon, Computer Solution of Ordinary Differential Equations: The Initial Value Problem, W.H. Freeman and Co., San Francisco, 1975.

